Accepted to ApJ: November 19, 2016
Preprint typeset using LaTeX style emulateapj v. 01/23/15

arXiv:1611.06976v2 [astro-ph.SR] 22 Nov 2016

EXTERNALLY HEATED PROTOSTELLAR CORES IN THE OPHIUCHUS STAR-FORMING REGION*

Johan E. Lindberg[1], Steven B. Charnley[1], Jes K. Jørgensen[2], Martin A. Cordiner[1,3], Per Bjerkeli[2,4]
[1]NASA Goddard Space Flight Center, Astrochemistry Laboratory, Mail Code 691, 8800 Greenbelt Road, Greenbelt, MD 20771, USA, johan.lindberg@nasa.gov
[2]Centre for Star and Planet Formation, Niels Bohr Institute and Natural History Museum of Denmark, University of Copenhagen, Øster Voldgade 5-7, DK-1350 Copenhagen K, Denmark
[3]Department of Physics, Catholic University of America, Washington, DC 20064, USA and
[4]Department of Earth and Space Sciences, Chalmers University of Technology, Onsala Space Observatory, 439 92 Onsala, Sweden
Accepted to ApJ: *November 19, 2016*

ABSTRACT

We present APEX 218 GHz observations of molecular emission in a complete sample of embedded protostars in the Ophiuchus star-forming region. To study the physical properties of the cores, we calculate H_2CO and c-C_3H_2 rotational temperatures, both of which are good tracers of the kinetic temperature of the molecular gas. We find that the H_2CO temperatures range between 16 K and 124 K, with the highest H_2CO temperatures toward the *hot corino* source IRAS 16293-2422 (69–124 K) and the sources in the ρ Oph A cloud (23–49 K) located close to the luminous Herbig Be star S 1, which externally irradiates the ρ Oph A cores. On the other hand, the c-C_3H_2 rotational temperature is consistently low (7–17 K) in all sources. Our results indicate that the c-C_3H_2 emission is primarily tracing more shielded parts of the envelope whereas the H_2CO emission (at the angular scale of the APEX beam; 3600 au in Ophiuchus) mainly traces the outer irradiated envelopes, apart from in IRAS 16293-2422, where the *hot corino* emission dominates. In some sources, a secondary velocity component is also seen, possibly tracing the molecular outflow.

Subject headings: stars: formation — ISM: molecules — ISM: individual objects (Ophiuchus) — astrochemistry — radiative transfer

1. INTRODUCTION

Low-mass protostars form from the collapse of dense molecular clouds. In their youngest stages, such protostars are deeply embedded in an envelope of dust and gas. Investigations of molecular emission lines of this envelope can be used to study both chemical and physical characteristics of the protostar. The temperature of the large-scale envelope is generally low ($\sim$ 10–15 K; e.g. Bergin & Tafalla 2007), but parts of the envelope can be heated by irradiation from the protostar itself or by external sources.

Molecular emission lines of H_2CO with the same J_u quantum number can be used as a probe of the kinetic temperature for cool ($T \lesssim 50$ K) gas at densities $\gtrsim 10^5$ cm^{-3} (Mangum & Wootten 1993). Through an unbiased survey of H_2CO toward embedded sources in the Corona Australis (CrA) star-forming region it was possible to characterize the temperature and external irradiation of such protostars, identifying the Herbig Be star R CrA as the dominant source of irradiation in CrA, heating nearby envelopes to temperatures $\sim$ 40 K, but also influencing the temperature on scales of a few 10 000 au (Lindberg et al. 2015). The same molecular transitions were used by Lindberg & Jørgensen (2012) to produce an interferometric map of the physical characteristics in the R CrA cloud (which hosts a handful of embedded low-mass protostars). The rotational temperatures of H_2CO were found to exceed 40 K across the whole cloud ($\sim$ 6000 au), consistent with *Herschel*/PACS observations of the extended dust temperature (Lindberg et al. 2014). In particular, strong H_2CO and CH_3OH emission with high temperatures and column densities was detected toward two long ($\sim$ 5000 au) ridges north and south of the low-mass young stellar objects (YSOs), whereas only faint H_2CO emission was detected toward the YSOs themselves. On the other hand, most of the fainter c-C_3H_2 emission was detected from the region between the two ridges. The S/N level of the observations was too low to establish c-C_3H_2 rotational temperatures, but in single-dish APEX observations the rotational temperature of c-C_3H_2 was found to be consistently low ($\sim$ 10 K) toward the embedded protostars in CrA (Lindberg et al. 2015).

The Ophiuchus star-forming region, at a distance of only 125 pc (de Geus et al. 1989; Wilking et al. 2008), is an excellent laboratory to test the knowledge gained from the CrA survey on a region with a greater number of potential heating sources, but also a greater separation between the low-mass sources, allowing for a distinction between effects from internal and external heating. The population of deeply embedded protostars was surveyed by Jørgensen et al. (2008) and Enoch et al. (2009) using *Spitzer* and JCMT/SCUBA continuum observations, and in combination, the two surveys identified 38 Class 0 and Class I protostars.

Kamegai et al. (2003) found large-scale elevated [C I] excitation temperatures in the ρ Oph A cloud using the Mount Fuji submillimeter telescope, and identified the B2 star HD 147889 as the heating source. Liseau et al. (2015), however, concluded that HD 147889 and the B4 star S 1 (also known as GSS 35) both influence the temperature of the cloud, but that S 1, despite being less

* Based on observations with the Atacama Pathfinder EXperiment (APEX) telescope. APEX is a collaboration between the Max Planck Institute for Radio Astronomy, the European Southern Observatory, and the Onsala Space Observatory.

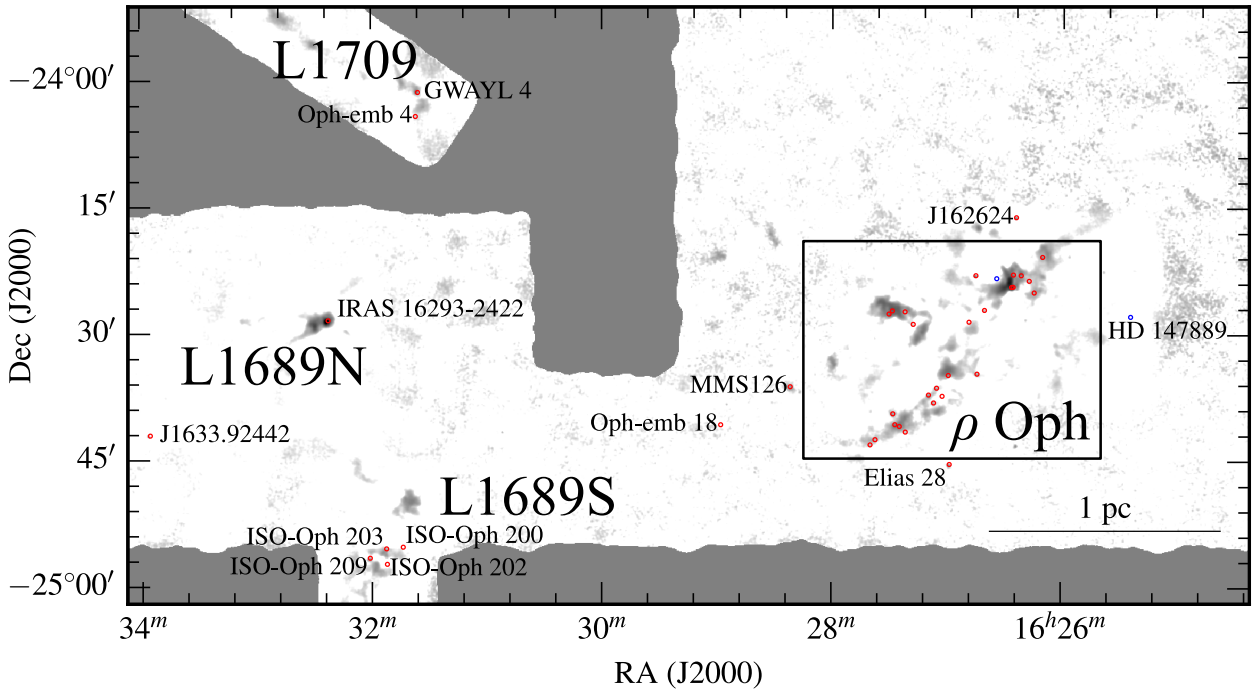

FIG. 1.— SCUBA 850 μm image of the Ophiuchus star-forming region (Johnstone et al. 2004). The uniformly gray areas were not covered by the SCUBA map. The sources targeted in this study are shown with red rings. In addition, the two luminous stars S 1 and HD 147889 are shown with blue rings. The area in the rectangle (ρ Oph) is shown at a larger scale in Figure 2.

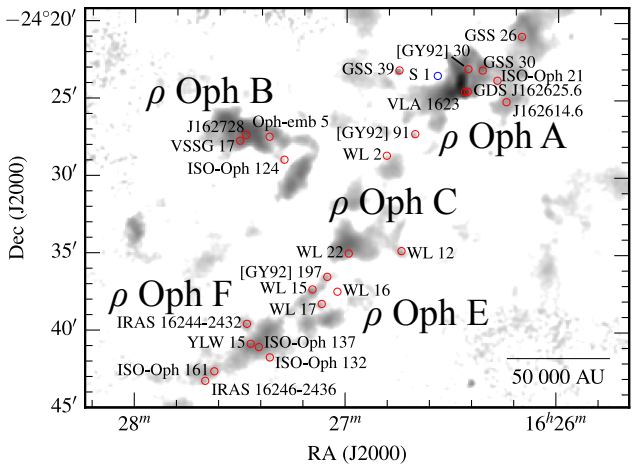

FIG. 2.— Zoom-in of the ρ Oph cloud in Figure 1. The sources targeted in this study are shown with red rings. The luminous source S 1 is shown with a blue ring. The size of the rings represent the APEX beam size of 29″.

luminous, is the more dominant heating source owing to its proximity to the ρ Oph A cloud. Here, we investigate the influence these luminous stars have on the physical properties of the molecular gas in nearby embedded protostars through 218 GHz spectral line observations.

2. OBSERVATIONS

Our observations were executed with the APEX (Atacama Pathfinder Experiment) 12 m telescope (Güsten et al. 2006) in position-switching mode in August and October 2014 and May 2015. The SHeFI APEX-1 receiver (Vassilev et al. 2008) was used to cover the frequency range 216–220 GHz toward a complete sample of the 38 deeply embedded protostellar sources in the Ophiuchus star-forming region. The sample consists of all embedded protostellar sources in the region detected by Jørgensen et al. (2008) and Enoch et al. (2009), see Table 1 and Figures 1–2. The spectral setup was chosen to cover three H_2CO spectral lines at 218 GHz, and also several spectral lines of c-C_3H_2, an abundant tracer of unsaturated hydrocarbon molecules.

We note that five of the sources in the sample (GSS 26, GSS 39, Elias 28, J162624, and J1633.92442) should be considered Class II sources by both the $T_{\rm bol} > 650$ K and the $\alpha_{\rm IR} < -0.3$ criteria (Evans et al. 2009), but are still included in the sample of embedded protostars of Jørgensen et al. (2008) due to their proximity ($< 15''$) to a SCUBA core. We detect no line emission toward one of these sources (J1633.92442) and only $C^{18}O$ line emission toward two (GSS 39 and Elias 28), and these sources are thus likely not deeply embedded. GSS 26 and J162624, however, show H_2CO line emission, indicating the presence of dense molecular gas. Finally, toward the two Class I sources WL16 and Oph-emb 4, we only detect emission from $C^{18}O$.

To remove quasi-sinusoidal baselines present in the APEX-1 spectra (see Vassilev et al. 2008), we used our running-mean script described in Appendix A of Lindberg et al. (2015). The spectra were thereafter reduced with the X-Spec package[2], which was used to average scans, perform Gaussian fits, and calculate line intensities. Throughout the paper we use the $T_{\rm mb}$ temperature scale, assuming a main beam efficiency $\eta_{\rm mb} = 0.75$.

[2] X-Spec is developed at Onsala Space observatory, and can be obtained from http://www.chalmers.se/en/centres/oso/radio-astronomy/Pages/software.aspx

TABLE 1
Coordinates and other properties of the observed sources

Cloud Source	R.A. (J2000.0)	Dec. (J2000.0)	Our rms [mK (km s^{-1})$^{-1}$]	$T_{\rm bol}$ [K]	$L_{\rm bol}$ [$L_\odot$]	$\alpha_{\rm IR}$	Other common identifiers
ρ Oph A							
GDS J162625.6	16:26:25.62	−24:24:28.9	15.0	< 72	> 0.039	1.65	
GSS 26	16:26:10.33	−24:20:54.8	26.6	920	0.3	−0.46	
GSS 30	16:26:21.42	−24:23:06.4	13.9	150	8.7	1.46	Elias 21
GSS 39	16:26:45.03	−24:23:07.7	24.6	970	0.23	−0.64	Elias 27
[GY92] 30	16:26:25.49	−24:23:01.6	12.0	135	0.10	0.87	
[GY92] 91	16:26:40.47	−24:27:14.5	16.9	< 370	> 0.065	0.45	CRBR42
ISO-Oph 21	16:26:17.23	−24:23:45.4	13.7	490	0.083	0.69	CRBR12
J162614.6	16:26:14.62	−24:25:08.4	14.7	...	...	...	
VLA 1623	16:26:26.42	−24:24:30.0	16.2	57	0.41	1.65	
ρ Oph B							
ISO-Oph 124	16:27:17.57	−24:28:56.3	15.1	68	2.6	0.25	
J162728	16:27:28.45	−24:27:21.0	13.3	310	0.48	−0.03	IRS45, [GY92] 273
Oph-emb 5	16:27:21.83	−24:27:27.6	13.1	180	0.019	−0.05	
VSSG 17	16:27:30.18	−24:27:43.4	15.2	530	0.93	−0.12	Elias 33, IRS47, [GY92] 279
ρ Oph C							
WL 2	16:26:48.49	−24:28:38.9	22.6	430	0.12	0.02	[GY92] 128
WL 12	16:26:44.19	−24:34:48.3	30.5	290	1.1	2.49	ISO-Oph 65
WL 22	16:26:59.17	−24:34:58.8	14.2	110	1.5	1.99	ISO-Oph 90
ρ Oph E							
[GY92] 197	16:27:05.25	−24:36:29.8	20.5	110	0.15	1.27	LFAM26
WL 15	16:27:09.43	−24:37:18.8	27.3	260	18	1.69	Elias 29, [GY92] 214
WL 16	16:27:02.34	−24:37:27.2	23.9	320	4.8	1.53	[GY92] 182
WL 17	16:27:06.78	−24:38:15.0	26.6	310	0.60	0.61	[GY92] 205
ρ Oph F							
IRAS 16244-2432	16:27:28.03	−24:39:33.5	26.3	110	15	2.29	IRS44, [GY92] 269
IRAS 16246-2436	16:27:39.83	−24:43:15.1	13.6	570	0.71	−0.15	IRS51,[GY92] 315
ISO-Oph 132	16:27:21.47	−24:41:43.1	25.0	600	1.2	−0.03	[GY92] 252
ISO-Oph 137	16:27:24.61	−24:41:03.4	25.9	191	0.33	1.01	CRBR85
ISO-Oph 161	16:27:37.25	−24:42:38.0	25.9	450	0.13	0.13	[GY92] 301
YLW 15	16:27:26.94	−24:40:50.8	24.3	160	3.8	1.17	IRS 43, [GY92] 265
L1689N							
IRAS 16293-2422	16:32:22.56	−24:28:31.8	12.5	47	16	5.03	
L1689S							
ISO-Oph 200	16:31:43.75	−24:55:24.6	24.9	500	0.28	0.23	
ISO-Oph 202	16:31:52.06	−24:57:26.0	26.2	< 120	> 0.0093	0.82	
ISO-Oph 203	16:31:52.45	−24:55:36.2	10.9	240	0.13	1.07	
ISO-Oph 209	16:32:01.00	−24:56:42.0	26.4	130	4.0	1.39	L1689S1, IRS67
L1709							
GWAYL 4	16:31:35.65	−24:01:29.3	24.1	300	1.4	0.14	IRAS 16285-2355
Oph-emb 4	16:31:36.80	−24:04:20.1	27.8	77	0.18	−0.27	
Solitary sources							
Elias 28	16:26:58.44	−24:45:31.9	24.1	860	1.2	−0.86	SR 24N
J162624	16:26:24.07	−24:16:13.5	25.0	980	1.9	−0.71	Elias 24
J1633.92442	16:33:55.61	−24:42:05.0	23.4	1500	0.17	−1.22	
MMS126	16:28:21.61	−24:36:23.4	14.9	41	0.29	1.23	IRAS 16253-2429
Oph-emb 18	16:28:57.85	−24:40:54.9	19.7	300	0.03	0.67	

Note. — Spectral properties from Evans et al. (2009), except for the values of [GY92] 30, VLA 1623, and ISO-Oph 137, which are from Enoch et al. (2009).

3. SPECTRAL LINE PROFILES

The spectral lines which were used in the analysis are listed in Table 2. These lines were not detected toward all sources, and in addition to these lines, several other lines (of e.g. C_2D, DCN, $C^{18}O$, $C^{33}S$, and HNCO) were detected in some of the sources, but will not be discussed in this paper. All observed line parameters are listed in Table 4 in Appendix A.

To enable comparison of the line profiles, Figure 3 shows the normalized spectra for the strongest DCO^+ (216.113 GHz), c-C_3H_2 (217.822 GHz), H_2CO (218.222 GHz), and SO (219.949 GHz) lines in each source where they have been detected. We note that for some sources, the line profiles of different molecular species are dramatically discrepant. In several cases, a double peak is seen in some spectral lines. The CH_3OH line (not plotted) is generally well-correlated with the H_2CO line shape, while C_2D (not plotted) correlates well with c-C_3H_2, although the C_2D line doublet makes analysis of the line profile non-trivial. Of the plotted lines, we find that the line profiles often separate the molecular species into two groups: H_2CO and SO on one hand, and c-C_3H_2 and DCO^+ on the other. Lindberg et al. (2015) found that H_2CO and other saturated organic species as well as SO and other sulfur-bearing species had significantly higher rotational temperatures than c-C_3H_2 and other unsaturated hydrocarbons in the APEX observations of the embedded protostar R CrA IRS7B. Like in CrA, the H_2CO and SO line profiles are generally wider than the c-C_3H_2 line profiles. This is also similar to the six molecular cores studied by Buckle et al. (2006), where CH_3OH and SO were found to be spatially correlated, but separated from the unsaturated hydrocarbon HC_3N.

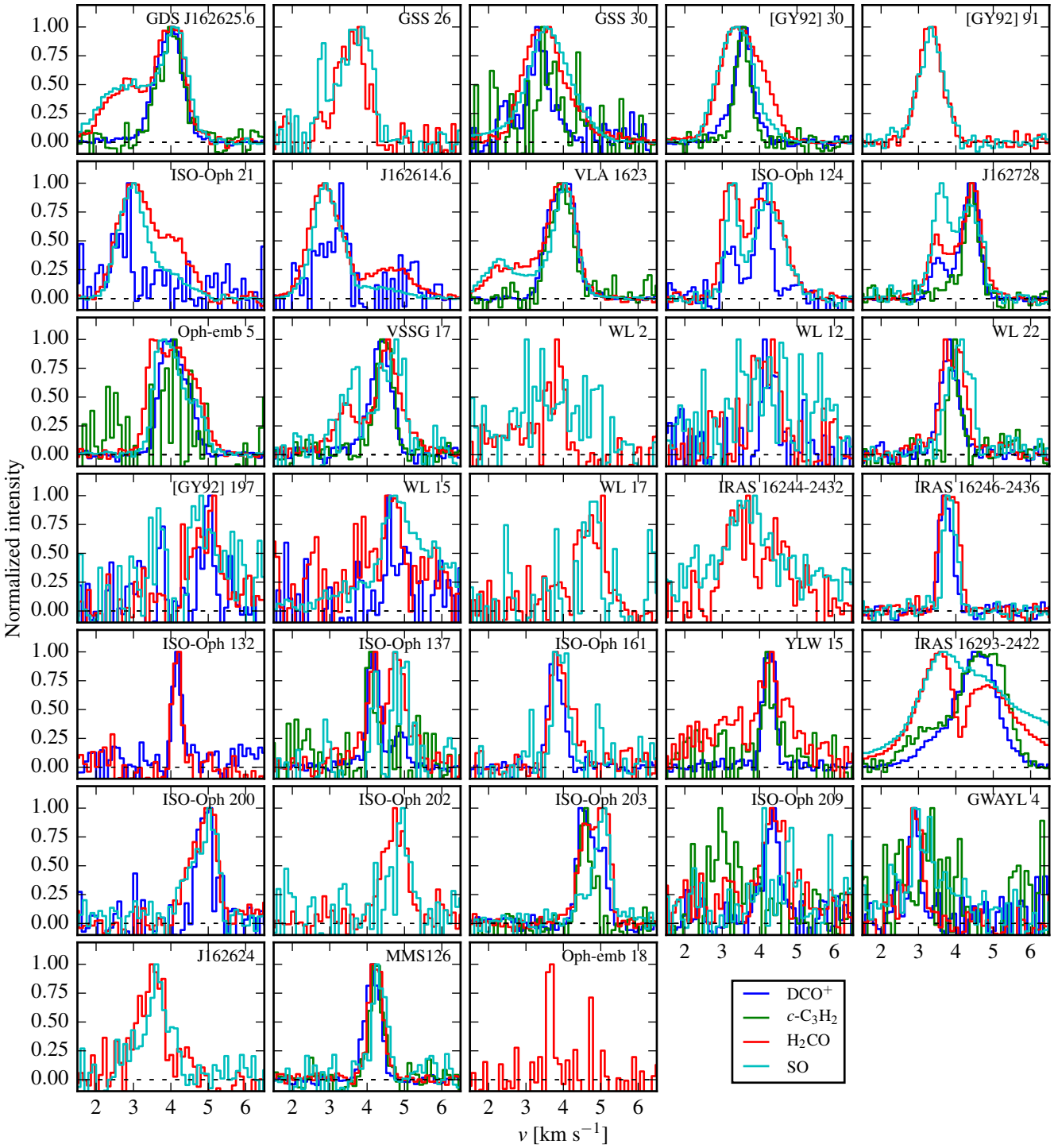

FIG. 3.— Spectra of the DCO$^+$ (216.113 GHz), c-C$_3$H$_2$ (217.822 GHz), H$_2$CO (218.222 GHz), and SO (219.949 GHz) lines for all sources in the sample for which at least one of these lines is detected at a 3σ level or higher (Elias 28, GSS 39, J1633.9-2442, Oph-emb 4, and WL 16 are not included since no such lines are detected), normalized to their individual peaks to facilitate comparison of the line profiles.

TABLE 2
Spectral lines used in the analysis

Molecule	Quantum numbers	Frequency [GHz]	Type	E_u/k [K]
DCO^+	$3 \rightarrow 2$	216.11258	...	20.7
c-C_3H_2	$3_{03} \rightarrow 2_{02}$	216.27876	ortho	19.5
c-C_3H_2	$6_{06} \rightarrow 5_{15}$	217.82215	para	38.6
c-C_3H_2	$6_{16} \rightarrow 5_{05}$	217.82215	ortho	38.6
c-C_3H_2	$5_{14} \rightarrow 4_{23}$	217.94005	ortho	35.4
c-C_3H_2	$5_{24} \rightarrow 4_{13}$	218.16046	para	35.4
H_2CO	$3_{03} \rightarrow 2_{02}$	218.22219	para	21.0
CH_3OH	$4_2 \rightarrow 3_1$	218.44006	E	45.5
H_2CO	$3_{22} \rightarrow 2_{21}$	218.47563	para	68.1
c-C_3H_2	$7_{16} \rightarrow 7_{07}$	218.73273	ortho	61.2
c-C_3H_2	$7_{26} \rightarrow 7_{17}$	218.73273	para	61.2
H_2CO	$3_{12} \rightarrow 2_{11}$	218.76007	para	68.1
SO	$6_5 \rightarrow 5_4$	219.94944	...	35.0

Note. — Rest frequencies from the CDMS (Müller et al. 2001) and JPL (Pickett et al. 1998) molecular spectroscopy databases.

For completeness, the corresponding spectra for the Corona Australis survey are shown in Figure 8 of Appendix B.

3.1. *Secondary components*

In at least nine sources (four in ρ Oph A, three in ρ Oph B, one in L1689S, and IRAS 16293-2422), a secondary component to some of the emission lines is detected. This was also seen in two sources in the CrA survey: SMM2 and CrA-24. In all eleven cases, the additional component is characterized by strong H_2CO and CH_3OH emission, and often also SO, but faint or no emission from other species. In CrA, the component likely comes from an overlapping molecular outflow (Miettinen et al., in prep.). We note that the velocity of the secondary component is blueward of the main component in all ρ Oph A and ρ Oph B sources with the exception of ISO-Oph 21 and J162614.6.

To account for the possibly distinct nature of these secondary velocity components, they are treated separately from the main component in the rotational temperature analysis, and are plotted as red data points in all plots (although they are typically not the redward components). We identify which component to be considered "secondary" by investigating the molecular emission prevalent at those velocities – typically, the secondary component has little or no DCO^+ and c-C_3H_2 emission. The secondary component is often also wider than the main component, and usually appears at a velocity different from the typical velocity of other sources in the same cloud (thus possibly representing a molecular outflow). For the rotational diagram analysis (see below), emission from the two components were separated by performing Gaussian fits. We find that the secondary component in most cases has a higher H_2CO rotational temperature than the main component, in agreement with the CrA sources.

4. ROTATIONAL TEMPERATURES

For all sources where at least two H_2CO or c-C_3H_2 spectral lines were detected, the respective rotational temperatures (assuming LTE) have been calculated. We assume that the lines are optically thin, which is valid at the observed column densities (Lindberg et al. 2015). For sources with only one detected line of a certain species, an upper limit of the rotational temperature was calculated by use of upper limits on the non-detected line(s). The results are presented in Table 3.

The three observed H_2CO lines all have the same $J_u = 3$, and their rotational temperature is thus an excellent proxy for the kinetic temperature, but makes estimates of the column density more uncertain (Mangum & Wootten 1993; Lindberg et al. 2015). We estimate the beam-averaged H_2CO column densities by use of the non-LTE radiative transfer code RADEX (van der Tak et al. 2007) assuming an H_2 number density of $(8.9 \pm 1.0) \times 10^5$ cm^{-3} in all sources. This value was measured from observations of multiple H_2CO $J_u = 3$ and $J_u = 5$ lines toward the protostar R CrA IRS7B using non-LTE methods (RADEX), and is of the same order of magnitude as found in the other protostars in CrA where this value could be measured (Lindberg et al. 2015). All observed H_2CO lines are para lines, and an ortho-to-para ratio is therefore not important for the excitation analysis. However, such a ratio is necessary to calculate the total H_2CO column density, and for this purpose an ortho/para ratio of 1.6 is assumed (see Dickens & Irvine 1999; Jørgensen et al. 2005). For the c-C_3H_2 excitation analysis, an ortho/para ratio of 3 is assumed (see Lucas & Liszt 2000). Non-LTE RADEX models of c-C_3H_2 show that its physical temperature is well-represented by the rotational temperature if $n(H_2) \gtrsim 10^5$ cm^{-3}, at temperatures typical for protostellar envelopes. This is further discussed in Appendix C (see also Spezzano et al. 2016).

The H_2CO rotational temperatures in the Ophiuchus star-forming region are generally higher than what is expected in low-mass protostars on the scale of the APEX primary beam (29″, or 3600 au at a distance of 125 pc). Internal heating by low-mass embedded protostars would produce temperatures $\sim$ 10–15 K on these scales (Bergin & Tafalla 2007). The H_2CO temperatures observed toward most sources thus require an external radiation field to be explained (see e.g. Jørgensen et al. 2006; Lindberg & Jørgensen 2012).

4.1. *IRAS 16293-2422*

The highest H_2CO rotational temperature in the survey was measured toward the Class 0 protostar IRAS 16293-2422 (69 ± 1 K in the main component and 124 ± 4 K in the secondary component). This source is the best studied example of a *hot corino* (see e.g. Cazaux et al. 2003; Caux et al. 2011), and as shown by interferometric observations, most of the line emission from organic species originates in the hot inner envelope ($R \lesssim 100$ au), where the central object heats the molecular gas to high temperatures (e.g. Bisschop et al. 2008). In contrast to the other sources in the survey (see below), which are not known to exhibit *hot corino* properties, the H_2CO temperature measured toward IRAS 16293-2422 likely traces the properties of this hot and dense inner envelope. Most other sources in the sample are also at a later stage of evolution than IRAS 16293-2422 as shown by their higher bolometric temperature.

However, the c-C_3H_2 temperatures measured toward IRAS 16293-2422 are much lower, only 14.4 ± 0.3 K and 16.5 ± 1.5 K for the main and secondary components, respectively, marginally higher than the values found in the other sources in the survey, thus likely tracing emission

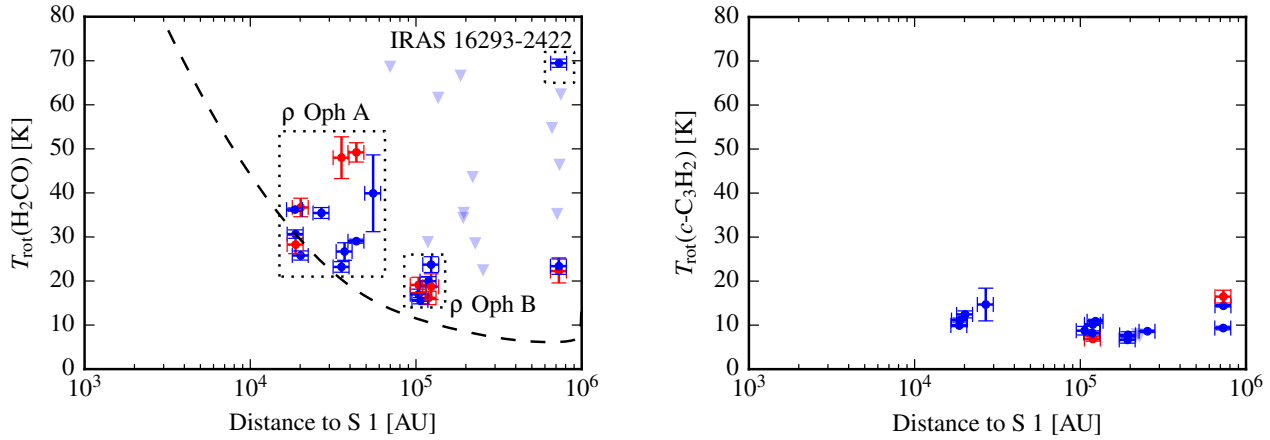

FIG. 4.— *Left:* H_2CO rotational temperature as function of the projected distance to the Herbig Be star S 1. Red data points represent the secondary component dominated by H_2CO, CH_3OH, and SO in sources with two line components, (see Section 3.1). The secondary component of IRAS 16293-2422 is off the scale, at 124 K. The dotted rectangles show sources belonging to the clouds ρ Oph A and ρ Oph B, and the *hot corino* IRAS 16293-2422. The black dashed curve shows a *Transphere* (Dullemond et al. 2002) model of the dust temperature resulting from the heating from S 1. The heating from the more luminous, although more distant, HD 147889 is not included since its contribution to the heating of most sources is minor in comparison with S 1 (see Figure 5). *Right:* c-C_3H_2 rotational temperature as function of the projected distance to the Herbig Be star S 1. In both figures, light-blue triangles are upper limits.

on larger scales.

4.2. *External heating of sources in ρ Oph A and ρ Oph B*

The H_2CO rotational temperatures are somewhat higher toward the sources in the ρ Oph A cloud than in the ρ Oph B cloud. With two exceptions (IRAS 16293-2422 and ISO-Oph 203), all sources where the H_2CO temperatures could be measured are located in these two clouds, and it is therefore not possibe to judge whether the H_2CO temperatures of these clouds are representative of protostellar envelopes in the whole region.

The luminous Herbig Be star S 1 is located only $2'$ ($\sim 15\,000$ au) east of ρ Oph A. It has spectral class B4 (Bouvier & Appenzeller 1992) and a luminosity $\sim$ 1000–1600$L_\odot$ (Bontemps et al. 2001; Wilking et al. 2005). About $15'$ (0.5 pc) west of the cloud lies the even more luminous B2 star HD 147889 (Houk & Smith-Moore 1988), with a luminosity $\sim 4500L_\odot$ (Greene & Young 1989). In their radiative transfer models, Liseau et al. (2015) use luminosities of S 1 and HD 147889 of $1100L_\odot$ and $4500L_\odot$, respectively.

In Figure 4, the rotational temperatures of H_2CO and c-C_3H_2 are plotted as a function of the projected distance to S 1. We also calculate how the luminous source S 1 influences the dust temperature, and thus indirectly the molecular gas temperature, using a 1-D *Transphere* model (Dullemond et al. 2002). We assume the luminosity of S 1 to be $1600L_\odot$ and a constant cloud density $n(H_2) = 10^4$ cm^{-3}. The model (dashed line in Figure 4) underpredicts the observed H_2CO temperatures of the sources in ρ Oph A and ρ Oph B somewhat, but the irradiation from HD 147889 and the internal irradiation from the embedded sources are not included in the model, which could account for the difference. A density different from our assumption, or a non-uniform density distribution within the cloud could also play a role in explaining the discrepancy.

To compare the contribution from the two heating

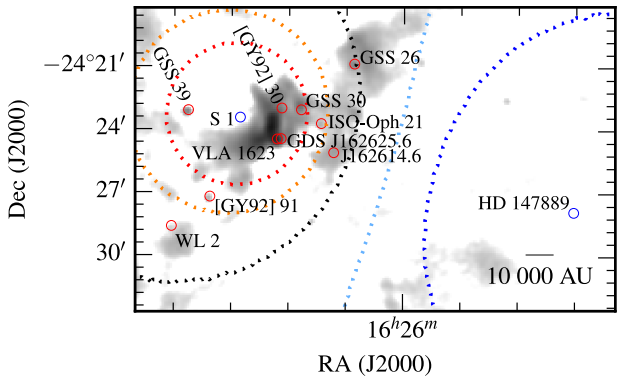

FIG. 5.— The black contour shows where the heating contributions of S 1 and HD 147889 are equal given our 1-D *Transphere* model assuming that all sources lie in the same plane of sky. The orange and red contours show the positions where the heating from only S 1 would produce temperatures 5 K and 10 K greater than the heating from only HD 147889. The light blue and dark blue contours show the corresponding positions for HD 147889.

sources, and to find the dominant source of heating in any given part of the cloud, Figure 5 shows where the heating from both sources are equal (black contour). This plot was made with two important assumptions limiting the level of interpretations to be made, namely that the cloud is uniformly dense ($n(H_2) = 10^4$ cm^{-3}) and that all sources lie in the same plane of sky.

4.3. *Temperatures of H_2CO and c-C_3H_2*

The H_2CO rotational temperature in the protostellar envelopes is strongly enhanced in the sources located close to the Herbig Be star S 1 and the very luminous star HD 147889, whereas the c-C_3H_2 rotational temperature is around 10–15 K in all sources (similar to the rotational temperatures of unsaturated hydrocarbon species observed in so-called warm carbon-chain chemistry sources, a type of deeply embedded protostars with high abundances of unsaturated carbon-chain molecules; see e.g. Sakai & Yamamoto 2013). The same trend is

TABLE 3
MEASURED ROTATIONAL TEMPERATURES, COLUMN DENSITIES, MEDIAN LINE WIDTHS, AND LSR VELOCITIES

Cloud / Source	H_2CO T_{rot} [K]	H_2CO N [10^{12} cm^{-2}]	H_2CO Δv [km s^{-1}]	H_2CO v_{LSR} [km s^{-1}]	c-C_3H_2 T_{rot} [K]	c-C_3H_2 N_{rot} [10^{12} cm^{-2}]	c-C_3H_2 Δv [km s^{-1}]	c-C_3H_2 v_{LSR} [km s^{-1}]
ρ Oph A								
GDS J162625.6 (main)	25.8 ± 1.0	18 ± 3	0.8	3.8	12.4 ± 0.8	2.5 ± 0.4	0.8	3.8
GDS J162625.6 (sec.)	36.7 ± 2.1	11 ± 1	1.4	2.6	...	...	...	...
GSS 26	39.9 ± 8.7	4.3 ± 1.4	1.1	3.4	...	...	...	...
GSS 30	35.4 ± 1.2	19 ± 2	1.3	3.3	14.7 ± 3.7	0.46 ± 0.26	0.9	3.5
GSS 39	...	...	...	...	...	...	...	...
[GY92] 30	36.2 ± 0.4	79 ± 8	1.2	3.4	9.9 ± 0.3	4.0 ± 0.3	0.4	3.4
[GY92] 91	26.7 ± 2.0	12 ± 2	0.6	3.2	...	...	...	...
ISO-Oph 21 (main)	23.2 ± 1.2	15 ± 3	0.9	2.8	...	...	...	...
ISO-Oph 21 (sec.)	48.0 ± 4.7	4.4 ± 0.6	1.2	3.9	...	...	...	...
J162614.6 (main)	29.0 ± 0.5	47 ± 6	0.9	2.7	...	...	...	...
J162614.6 (sec.)	49.2 ± 2.2	11 ± 1	1.5	4.3	...	...	...	...
VLA 1623 (main)	30.6 ± 1.0	23 ± 3	0.8	3.8	11.2 ± 0.5	4.2 ± 0.5	0.8	3.8
VLA 1623 (sec.)	28.3 ± 2.1	12 ± 2	1.4	2.5	...	...	...	...
ρ Oph B								
ISO-Oph 124 (main)	17.0 ± 1.2	23 ± 5	1.1	4.3	...	...	...	...
ISO-Oph 124 (sec.)	19.1 ± 1.7	9.2 ± 2.4	0.5	3.1	...	...	...	...
J162728 (main)	20.0 ± 1.1	21 ± 4	0.6	4.2	10.2 ± 0.2	4.1 ± 0.3	0.4	4.3
J162728 (sec.)	16.2 ± 1.5	13 ± 4	0.5	3.4	6.9 ± 0.5	1.9 ± 0.5	0.5	3.7
Oph-emb 5	15.5 ± 0.7	55 ± 12	0.8	3.7	8.7 ± 1.0	1.0 ± 0.4	0.5	3.9
VSSG 17 (main)	23.7 ± 1.8	12 ± 2	0.8	4.4	10.9 ± 0.4	3.2 ± 0.4	0.5	4.3
VSSG 17 (sec.)	18.7 ± 2.9	6.2 ± 2.4	0.5	3.3	...	...	...	...
ρ Oph C								
WL 2	< 120	...	0.5	3.7	...	...	...	...
WL 12	< 215	...	0.9	4.0	...	...	...	...
WL 22	< 28.8	...	0.8	3.8	8.2 ± 0.5	2.4 ± 0.5	0.4	3.8
ρ Oph E								
[GY92] 197	< 61.6	...	0.9	4.8	...	...	...	...
WL 15	< 109	...	2.2	4.5	...	...	...	...
WL 16	...	...	...	...	...	...	...	...
WL 17	< 292	...	0.9	4.6	...	...	...	...
ρ Oph F								
IRAS 16244-2432	< 66.6	...	1.9	3.7	...	...	...	...
IRAS 16246-2436	< 28.5	...	0.6	3.7	< 7.5	...	0.3	3.7
ISO-Oph 132	< 138	...	0.3	4.0	...	...	...	...
ISO-Oph 137	< 34.3	...	1.3	4.4	6.7 ± 0.8	2.5 ± 1.0	0.2	4.0
ISO-Oph 161	< 43.6	...	0.6	3.8	< 7.9	...	0.4	3.7
YLW 15	< 35.4	...	2.4	3.9	7.8 ± 0.7	2.6 ± 0.8	0.4	4.1
L1689N								
IRAS 16293-2422 (main)	69.4 ± 0.9	47 ± 3	2.7	4.8	14.4 ± 0.3	6.5 ± 0.3	1.3	4.6
IRAS 16293-2422 (sec.)	124 ± 3	32 ± 1	1.7	3.2	16.5 ± 1.5	2.4 ± 0.5	1.7	3.1
L1689S								
ISO-Oph 200	< 35.2	...	0.8	4.7	...	...	...	...
ISO-Oph 202	< 46.4	...	0.8	4.6	...	...	...	...
ISO-Oph 203 (main)	23.4 ± 1.9	5.9 ± 1.2	0.5	4.5	9.3 ± 0.4	1.9 ± 0.3	0.4	4.4
ISO-Oph 203 (sec.)	22.3 ± 2.7	4.0 ± 1.1	0.4	4.9	...	...	...	...
ISO-Oph 209	< 62.3	...	1.3	4.2	...	...	1.3	2.9
L1709								
GWAYL 4	< 54.7	...	0.5	2.8	...	...	1.3	3.0
Oph-emb 4	...	...	...	...	...	...	...	...
Solitary sources								
Elias 28	...	...	...	...	...	...	...	...
J162624	< 68.6	...	0.8	3.3	...	...	...	...
J1633.92442	...	...	...	...	...	...	...	...
MMS126	< 22.4	...	0.4	4.1	8.6 ± 0.3	4.4 ± 0.5	0.4	4.1
Oph-emb 18	...	...	0.2	3.5	...	...	...	...

NOTE. — The H_2CO column densities were calculated by non-LTE methods assuming $n(H_2) = (8.9 \pm 1.0) \times 10^5$ cm^{-3} (see Section 4). The linewidths and LSR velocities are median values. Section 3.1 describes the main and secondary components.

found in a similar study in the CrA star-forming region (Lindberg et al. 2015). For some reason, the H_2CO gas is more prone to be heated by external radiation fields, or the H_2CO abundance is enhanced in the irradiated gas, possibly due to photo-chemistry (see e.g Guzmán et al. 2011). We propose that the H_2CO emission originates in relatively outer regions of the envelope (on scales of $R \sim 2000$ au; toward the edge of the APEX beam) more exposed to the external irradiation field, while the c-C_3H_2 emission originates in inner regions of the envelope, where it is shielded against the external irradiation. This is consistent with interferometric observations of the externally irradiated protostar R CrA IRS7B, which show heated H_2CO in large structures a few 1000 au from the central low-mass objects, while the c-C_3H_2 is found closer to the protostars (Lindberg & Jørgensen 2012).

Surprisingly, the same differentiation in temperature between H_2CO and c-C_3H_2 is found toward

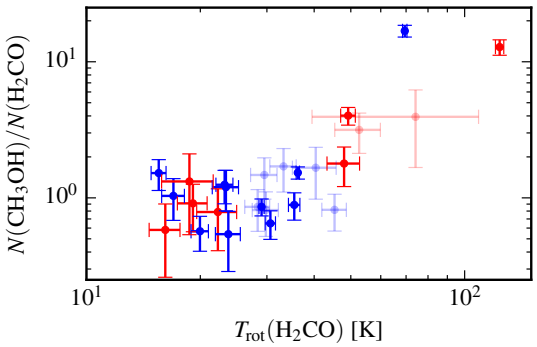

FIG. 6.— The CH_3OH/H_2CO column density is here plotted as a function of the H_2CO rotational temperature. The semi-transparent data points represent embedded sources in the CrA star-forming region (Lindberg et al. 2015). Red data points represent the secondary component dominated by H_2CO, CH_3OH, and SO in sources with two line components (see Section 3.1).

IRAS 16293-2422, where the high H_2CO temperature must have an internal origin (see above). The c-C_3H_2 gas likely also exists in this hot inner envelope, but the bulk of the emission possibly traces an intermediately deep region of the protostellar envelope, too deeply embedded to be heated by external irradiation, but also far from the internal heating source that gives rise to the *hot corino* chemistry of the inner 50–100 au of IRAS 16293-2422, where the temperature is > 100 K, making complex organic molecules as well as H_2CO evaporate from the icy grain mantles.

5. CORRELATIONS BETWEEN DIFFERENT SPECIES

In this section, to evaluate the statistical significance of any correlations, we use Spearman's ρ rank correlation test, which tests the monotonicity of two sets of variables without requiring a linear relation or a normal distribution of the variables. The H_2CO and c-C_3H_2 rotational temperatures and column densities are given in Table 3. The CH_3OH column densities were estimated using the CH_3OH line at 218.440 GHz and the H_2CO rotational temperature as a proxy for the CH_3OH rotational temperature. This assumption is based on the similar origin of these two molecules (hydrogenation of CO on grain mantles; see e.g. Charnley 1997), interferometric observations showing them to be spatially co-aligned in protostellar envelopes (e.g. Lindberg & Jørgensen 2012), and the similar critical densities of the observed H_2CO and CH_3OH lines (a few $\times$ 10^5 cm^{-3}; Guzmán et al. 2011, 2013). We used RADEX models to find that the CH_3OH line at 218.440 GHz is optically thin and that our method provides reliable values on the CH_3OH column density assuming $n \sim 10^6$ cm^{-3} and $T \lesssim 40$ K (see also Lindberg et al. 2016).

Lindberg et al. (2015) suggested a trend between the H_2CO rotational temperature and the CH_3OH/H_2CO ratio in the embedded protostars of CrA. In Figure 6 we plot the CH_3OH/H_2CO column density ratio as a function of the H_2CO rotational temperature, and find that they have a strong correlation (Spearman's rank test gives $\rho = 0.62$ with $p < 0.001$). If disregarding the data points of the *hot corino* source IRAS 16293-2422 (since the bulk of this emission should originate in the hot inner envelope), the correlation weakens somewhat ($\rho = 0.52$ with $p < 0.01$). However, if also disregarding the secondary components due to their uncertain origin, there is no significant correlation between the CH_3OH/H_2CO and the H_2CO rotational temperature. A correlation would be in agreement with laboratory results suggesting that the grain-surface hydrogenation reactions forming CH_3OH are more efficient at higher temperatures (e.g. Fuchs et al. 2009). The exact mechanism behind CH_3OH evaporation at low temperatures, however, remains unclear (Martín-Doménech et al. 2016; Bertin et al. 2016).

In Figure 7, we investigate the correlation between the rotational temperatures and column densities of H_2CO, CH_3OH, and c-C_3H_2. The CH_3OH column density was estimated assuming $T_{rot}(CH_3OH) = T_{rot}(H_2CO)$. We find no correlation between the H_2CO rotational temperature and column density ($\rho = 0.14$, $p \approx 0.44$), but the CH_3OH column density is moderately correlated with the H_2CO temperature ($\rho = 0.58$, $p \approx 0.001$), which indicates that CH_3OH production is enhanced by high temperatures or radiation fields (grain-mantle evaporation and/or enhancement of hydrogenation reactions on grain surfaces; cf. Öberg et al. 2009). If disregarding the *hot corino* source IRAS 16293-2422, the correlation is still significant ($\rho = 0.48$, $p < 0.02$). For c-C_3H_2 there is no significant correlation between its rotational temperature and column density (not plotted; $\rho = 0.19$, $p \approx 0.41$), which would suggest that its formation is not temperature-dependent. We find a very strong correlation between the H_2CO and CH_3OH column densities ($\rho = 0.82$, $p < 10^{-6}$) indicating that these molecules share a common origin (e.g. grain-mantle hydrogenation of CO). To exclude the possibility of this correlation being biased by the fact that we use the H_2CO temperature to find the CH_3OH column density we also performed this calculation assuming a fixed $T_{rot}(CH_3OH) = 10$ K for all sources, and still find a strong correlation between $N(H_2CO)$ and $N(CH_3OH)$. Finally, the c-C_3H_2 and H_2CO column densities show a barely significant correlation ($\rho = 0.52$, $p \approx 0.04$).

6. SUMMARY AND CONCLUSIONS

We find that the H_2CO temperature in protostellar cores depends strongly on the distance to external sources of strong irradiation, whereas the c-C_3H_2 temperature is insensitive to such irradiation (see Figure 4). This implies that the H_2CO traces the outer, externally irradiated layers of the protostellar cores, whereas the emission from c-C_3H_2 originates primarily in the inner, more shielded region. However, in the *hot corino* source IRAS 16293-2422, the majority of the c-C_3H_2 gas appears to mainly trace an intermediate region, shielded from any external irradiation, but sufficiently distant from the central protostar to remain relatively cool.

We also find that the column densities of the two molecules H_2CO and CH_3OH are closely related, suggesting that they share a common origin. Interferometric observations would be necessary to confirm that they spatially co-exist, and also to study the nature of the secondary components found toward many of the studied sources.

The chemical implications of external heating are still not well-understood. A comparative study using interferometric observations of similar protostars within the same star-forming region but with different levels of external irradiation could be used to investigate the origin

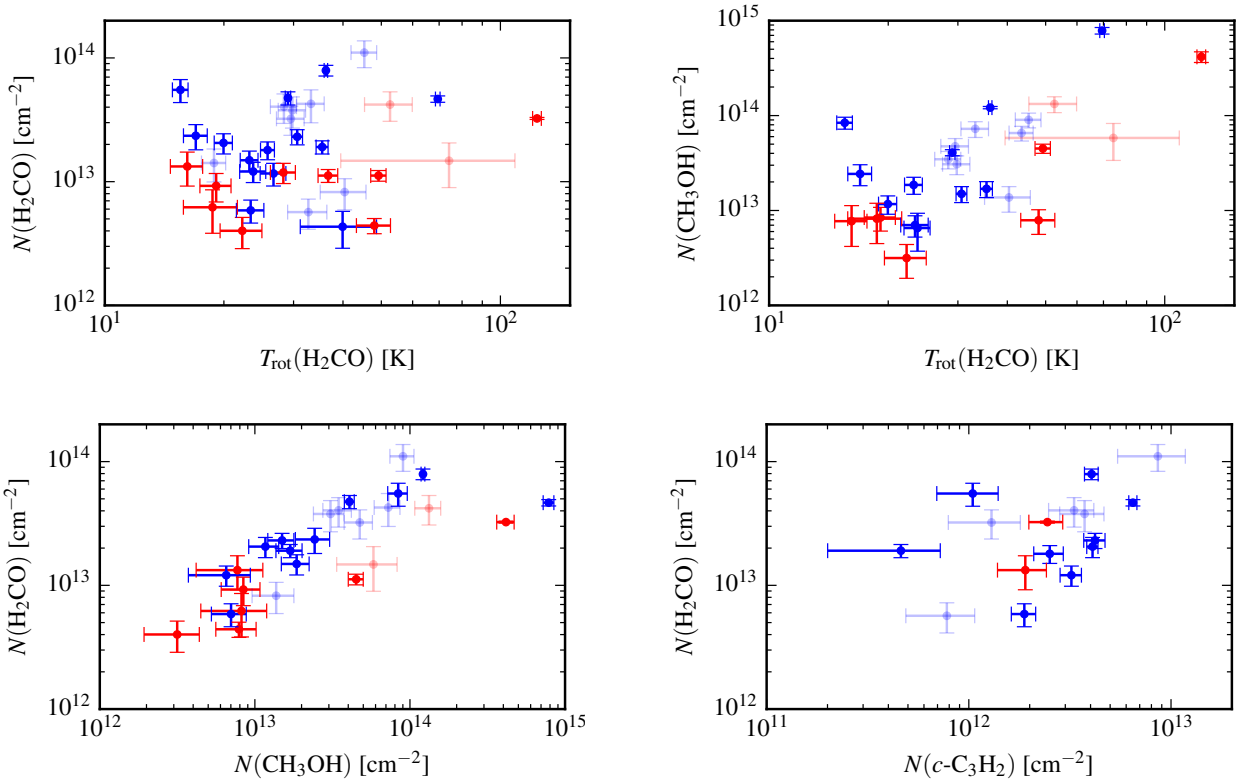

FIG. 7.— Plots studying trends between rotational temperatures and column densities of H_2CO, CH_3OH, and c-C_3H_2. The CH_3OH column density was estimated assuming $T_{rot}(CH_3OH) = T_{rot}(H_2CO)$. The semi-transparent data points represent similar embedded sources in the CrA star-forming region (Lindberg et al. 2015). Red data points represent the secondary component dominated by H_2CO, CH_3OH, and SO in sources with two line components (see Section 3.1).

of the differences in chemical composition and distribution. We suggest future line surveys searching for complex organic molecules and hydrocarbon species, and interferometric mapping of a few key species in the most luminous sources of ρ Oph A and ρ Oph B.

This research was supported by NASA's Emerging Worlds Program and by an appointment to the NASA Postdoctoral Program at the NASA Goddard Space Flight Center to J.E.L., administered by Universities Space Research Association through a contract with NASA. We thank the anonymous referee for insightful comments and suggestions which helped us improve the manuscript.

REFERENCES

Bergin, E. A., & Tafalla, M. 2007, ARA&A, 45, 339
Bertin, M., Romanzin, C., Doronin, M., et al. 2016, ApJ, 817, L12
Bisschop, S. E., Jørgensen, J. K., Bourke, T. L., Bottinelli, S., & van Dishoeck, E. F. 2008, A&A, 488, 959
Bontemps, S., André, P., Kaas, A. A., et al. 2001, A&A, 372, 173
Bouvier, J., & Appenzeller, I. 1992, A&AS, 92, 481
Buckle, J. V., Rodgers, S. D., Wirström, E. S., et al. 2006, Faraday Discussions, 133, 63
Caux, E., Kahane, C., Castets, A., et al. 2011, A&A, 532, A23
Cazaux, S., Tielens, A. G. G. M., Ceccarelli, C., et al. 2003, ApJ, 593, L51
Chandra, S., & Kegel, W. H. 2000, A&AS, 142, 113
Charnley, S. B. 1997, in IAU Colloq. 161: Astronomical and Biochemical Origins and the Search for Life in the Universe, ed. C. Batalli Cosmovici, S. Bowyer, & D. Werthimer, Vol. 161, 89
de Geus, E. J., de Zeeuw, P. T., & Lub, J. 1989, A&A, 216, 44
Dickens, J. E., & Irvine, W. M. 1999, ApJ, 518, 733
Dullemond, C. P., van Zadelhoff, G. J., & Natta, A. 2002, A&A, 389, 464
Enoch, M. L., Evans, II, N. J., Sargent, A. I., & Glenn, J. 2009, ApJ, 692, 973
Evans, II, N. J., Dunham, M. M., Jørgensen, J. K., et al. 2009, ApJS, 181, 321
Fuchs, G. W., Cuppen, H. M., Ioppolo, S., et al. 2009, A&A, 505, 629
Greene, T. P., & Young, E. T. 1989, ApJ, 339, 258
Güsten, R., Nyman, L. Å., Schilke, P., et al. 2006, A&A, 454, L13
Guzmán, V., Pety, J., Goicoechea, J. R., Gerin, M., & Roueff, E. 2011, A&A, 534, A49
Guzmán, V. V., Goicoechea, J. R., Pety, J., et al. 2013, A&A, 560, A73
Houk, N., & Smith-Moore, M. 1988, Michigan Catalogue of Two-dimensional Spectral Types for the HD Stars. Volume 4, Declinations −26°.0 to −12°.0. (Department of Astronomy, University of Michigan, Ann Arbor, MI 48109-1090, USA)
Johnstone, D., Di Francesco, J., & Kirk, H. 2004, ApJ, 611, L45
Jørgensen, J. K., Johnstone, D., Kirk, H., et al. 2008, ApJ, 683, 822
Jørgensen, J. K., Johnstone, D., van Dishoeck, E. F., & Doty, S. D. 2006, A&A, 449, 609
Jørgensen, J. K., Schöier, F. L., & van Dishoeck, E. F. 2002, A&A, 389, 908
—. 2005, A&A, 437, 501
Kamegai, K., Ikeda, M., Maezawa, H., et al. 2003, ApJ, 589, 378
Lindberg, J. E., Charnley, S. B., & Cordiner, M. A. 2016, ApJ, in press, arXiv:1611.06975

Lindberg, J. E., & Jørgensen, J. K. 2012, A&A, 548, A24
Lindberg, J. E., Jørgensen, J. K., Green, J. D., et al. 2014, A&A, 565, A29
Lindberg, J. E., Jørgensen, J. K., Watanabe, Y., et al. 2015, A&A, 584, A28
Liseau, R., Larsson, B., Lunttila, T., et al. 2015, A&A, 578, A131
Lucas, R., & Liszt, H. S. 2000, A&A, 358, 1069
Mangum, J. G., & Wootten, A. 1993, ApJS, 89, 123
Martín-Doménech, R., Muñoz Caro, G. M., & Cruz-Díaz, G. A. 2016, A&A, 589, A107
Müller, H. S. P., Thorwirth, S., Roth, D. A., & Winnewisser, G. 2001, A&A, 370, L49
Öberg, K. I., Garrod, R. T., van Dishoeck, E. F., & Linnartz, H. 2009, A&A, 504, 891
Pickett, H. M., Poynter, R. L., Cohen, E. A., et al. 1998, J. Quant. Spec. Radiat. Transf., 60, 883
Sakai, N., & Yamamoto, S. 2013, Chemical Reviews, 113, 8981
Schöier, F. L., van der Tak, F. F. S., van Dishoeck, E. F., & Black, J. H. 2005, A&A, 432, 369
Spezzano, S., Gupta, H., Brünken, S., et al. 2016, A&A, 586, A110
van der Tak, F. F. S., Black, J. H., Schöier, F. L., Jansen, D. J., & van Dishoeck, E. F. 2007, A&A, 468, 627
Vassilev, V., Meledin, D., Lapkin, I., et al. 2008, A&A, 490, 1157
Wilking, B. A., Gagné, M., & Allen, L. E. 2008, Star Formation in the ρ Ophiuchi Molecular Cloud, ed. B. Reipurth, 351
Wilking, B. A., Meyer, M. R., Robinson, J. G., & Greene, T. P. 2005, AJ, 130, 1733

APPENDIX

A. OBSERVED LINE PARAMETERS

Table 4 lists the detected lines in all observed sources. The errors on integrated intensities are 1σ rms errors. In a few of the sources we found that considerable $C^{18}O$ emission in the off-position made the $C^{18}O$ line data unreliable for those sources. Those are indicated by "Off-em." in their integrated intensity column. We do not expect any of the other lines, which are much fainter (in particular in the diffuse gas where the off-positions were measured), to be affected by off-position emission.

In sources with two components, these are listed as separate sources. LSR velocities and line widths are from Gaussian fits. For the sources with two components, the integrated intensities are from Gaussian fits. In all other sources, they are integrated over the whole spectral line.

TABLE 4
MEASURED LINE PARAMETERS

Source Rest freq. [MHz]	Molecule	Transition	$v_{\rm LSR}$ [km s^{-1}]	Δv [km s^{-1}]	$\int T_{\rm mb} dv$ [K km s^{-1}]
GDS J162625.6 (main)					
216112.58	DCO^+	$J = 3$–2	3.8	0.8	3.84 ± 0.03
216278.76	c-C_3H_2	3_{03}–2_{21}	3.8	0.8	0.28 ± 0.02
216373.32	C_2D	$N = 3$–2, $J = 7/2$–$5/2$[a]	4.0	1.3	0.48 ± 0.03
216428.32	C_2D	$N = 3$–2, $J = 5/2$–$3/2$[b]	3.6	1.0	0.28 ± 0.02
217238.54	DCN	$J = 3$–2	3.8	1.1	0.58 ± 0.03
217822.15	c-C_3H_2	6_{06}–5_{15}, 6_{16}–5_{05}	3.8	0.8	0.38 ± 0.03
217940.05	c-C_3H_2	5_{14}–4_{23}	3.8	0.7	0.22 ± 0.02
218160.46	c-C_3H_2	5_{24}–4_{13}	3.9	1.3	0.09 ± 0.02
218222.19	H_2CO	3_{03}–2_{02}	3.9	0.8	1.87 ± 0.02
218475.63	H_2CO	3_{22}–2_{21}	3.8	0.7	0.17 ± 0.02
218760.07	H_2CO	3_{21}–2_{20}	3.8	0.9	0.16 ± 0.02
219560.35	$C^{18}O$	$J = 2$–1	3.9	0.8	10.65 ± 0.02
219949.44	SO	6_5–5_4	4.0	0.7	1.45 ± 0.02
GDS J162625.6 (secondary)					
218222.19	H_2CO	3_{03}–2_{02}	2.7	1.4	1.56 ± 0.02
218475.63	H_2CO	3_{22}–2_{21}	2.6	1.7	0.28 ± 0.02
218760.07	H_2CO	3_{21}–2_{20}	2.5	1.3	0.18 ± 0.02
219560.35	$C^{18}O$	$J = 2$–1	3.0	1.6	9.76 ± 0.03
219949.44	SO	6_5–5_4	2.8	1.9	2.30 ± 0.03
GSS 26					
218222.19	H_2CO	3_{03}–2_{02}	3.4	0.9	0.65 ± 0.04
218475.63	H_2CO	3_{22}–2_{21}	3.2	1.7	0.12 ± 0.04
218760.07	H_2CO	3_{21}–2_{20}	3.6	1.1	0.10 ± 0.04
219560.35	$C^{18}O$	$J = 2$–1	3.4	1.6	19.40 ± 0.05
219949.44	SO	6_5–5_4	3.4	1.3	0.71 ± 0.03
GSS 30					
216112.58	DCO^+	$J = 3$–2	3.2	0.7	0.27 ± 0.02
216278.76	c-C_3H_2	3_{03}–2_{21}	3.4	0.4	0.05 ± 0.01
217104.98	SiO	$J = 5$–4	3.2	9.8	0.77 ± 0.06
217822.15	c-C_3H_2	6_{06}–5_{15}, 6_{16}–5_{05}	3.5	1.4	0.10 ± 0.02
217827.18	^{33}SO	6_5–5_4, $F = 9/2$–$7/2$	3.0	0.9	0.17 ± 0.02
217829.83	^{33}SO	6_5–5_4	3.0	1.2	0.25 ± 0.02
217831.77	^{33}SO	6_5–5_4[c]	2.9	1.4	0.50 ± 0.02
218222.19	H_2CO	3_{03}–2_{02}	3.3	1.3	2.52 ± 0.03
218324.72	HC_3N	$J = 24$–23	3.1	0.3	0.03 ± 0.01
218440.06	CH_3OH	4_2–3_1, E	3.1	1.1	0.10 ± 0.02
218475.63	H_2CO	3_{22}–2_{21}	3.3	1.3	0.41 ± 0.02
218760.07	H_2CO	3_{21}–2_{20}	3.4	1.3	0.28 ± 0.03
219166.24	CCO	$N = 10$–9, $J = 9$–9	2.3	1.1	0.22 ± 0.02
219355.01	$^{34}SO_2$	$11_{1,11}$–$10_{0,10}$	3.1	1.1	0.33 ± 0.02
219560.35	$C^{18}O$	$J = 2$–1	3.3	1.6	16.20 ± 0.03
219949.44	SO	6_5–5_4	3.4	1.4	15.40 ± 0.03
GSS 39					
219560.35	$C^{18}O$	$J = 2$–1	...	...	Off-em.
[GY92] 30					
216112.58	DCO^+	$J = 3$–2	3.4	0.6	1.03 ± 0.02
216278.76	c-C_3H_2	3_{03}–2_{21}	3.4	0.4	0.42 ± 0.01
216373.32	C_2D	$N = 3$–2, $J = 7/2$–$5/2$[a]	3.8	1.3	0.24 ± 0.02
216428.32	C_2D	$N = 3$–2, $J = 5/2$–$3/2$[b]	3.2	1.1	0.14 ± 0.02
217238.54	DCN	$J = 3$–2	3.3	1.0	0.31 ± 0.02
217822.15	c-C_3H_2	6_{06}–5_{15}, 6_{16}–5_{05}	3.4	0.5	0.39 ± 0.02
217940.05	c-C_3H_2	5_{14}–4_{23}	3.4	0.4	0.24 ± 0.01

TABLE 4 — *Continued*

Source Rest freq. [MHz]	Molecule	Transition	$v_{\rm LSR}$ [km s^{-1}]	Δv [km s^{-1}]	$\int T_{\rm mb} dv$ [K km s^{-1}]
218160.46	c-C_3H_2	5_{24}–4_{13}	3.4	0.3	0.08 ± 0.01
218222.19	H_2CO	3_{03}–2_{02}	3.4	1.3	8.01 ± 0.03
218440.06	CH_3OH	4_2–3_1, E	3.3	1.1	0.72 ± 0.02
218475.63	H_2CO	3_{22}–2_{21}	3.3	1.2	1.25 ± 0.02
218760.07	H_2CO	3_{21}–2_{20}	3.4	1.2	1.18 ± 0.02
219560.35	$C^{18}O$	$J = 2$–1	3.3	1.3	19.50 ± 0.03
219798.27	HNCO	$10_{0,10}$–$9_{0,9}$	3.2	0.8	0.07 ± 0.01
219908.52	$H_2^{13}CO$	3_{12}–2_{11}	3.4	1.2	0.23 ± 0.02
219949.44	SO	6_5–5_4	3.2	1.1	8.26 ± 0.02
[GY92] 91					
218222.19	H_2CO	3_{03}–2_{02}	3.2	0.7	1.29 ± 0.03
218475.63	H_2CO	3_{22}–2_{21}	3.1	0.6	0.10 ± 0.02
218760.07	H_2CO	3_{21}–2_{20}	3.2	0.6	0.14 ± 0.02
219560.35	$C^{18}O$	$J = 2$–1	...	...	Off-em.
219949.44	SO	6_5–5_4	3.2	0.8	0.64 ± 0.02
ISO-Oph 21 (main)					
216112.58	DCO^+	$J = 3$–2	2.5	0.8	0.12 ± 0.02
218222.19	H_2CO	3_{03}–2_{02}	2.8	1.0	1.50 ± 0.02
218440.06	CH_3OH	4_2–3_1, E	2.8	1.6	0.12 ± 0.02
218475.63	H_2CO	3_{22}–2_{21}	2.8	0.9	0.13 ± 0.02
218760.07	H_2CO	3_{21}–2_{20}	2.9	0.8	0.08 ± 0.02
219560.35	$C^{18}O$	$J = 2$–1	2.8	0.8	9.29 ± 0.02
219949.44	SO	6_5–5_4	2.8	0.8	2.89 ± 0.02
ISO-Oph 21 (secondary)					
218222.19	H_2CO	3_{03}–2_{02}	3.9	0.9	0.71 ± 0.02
218440.06	CH_3OH	4_2–3_1, E	4.1	0.4	0.04 ± 0.01
218475.63	H_2CO	3_{22}–2_{21}	4.0	1.2	0.16 ± 0.02
218760.07	H_2CO	3_{21}–2_{20}	3.9	1.4	0.14 ± 0.02
219560.35	$C^{18}O$	$J = 2$–1	4.1	1.0	5.59 ± 0.02
219949.44	SO	6_5–5_4	3.8	1.2	0.96 ± 0.02
J162614.6 (main)					
216112.58	DCO^+	$J = 3$–2	3.0	0.7	0.09 ± 0.02
218222.19	H_2CO	3_{03}–2_{02}	2.7	1.0	4.45 ± 0.02
218440.06	CH_3OH	4_2–3_1, E	2.8	1.0	0.26 ± 0.02
218475.63	H_2CO	3_{22}–2_{21}	2.7	0.9	0.54 ± 0.02
218760.07	H_2CO	3_{21}–2_{20}	2.7	0.8	0.42 ± 0.02
219560.35	$C^{18}O$	$J = 2$–1	2.7	0.9	10.95 ± 0.02
219908.52	$H_2^{13}CO$	3_{12}–2_{11}	2.9	0.7	0.09 ± 0.02
219949.44	SO	6_5–5_4	2.8	0.9	4.14 ± 0.02
J162614.6 (secondary)					
218222.19	H_2CO	3_{03}–2_{02}	4.4	1.5	1.79 ± 0.03
218440.06	CH_3OH	4_2–3_1, E	4.3	1.6	0.22 ± 0.02
218475.63	H_2CO	3_{22}–2_{21}	4.3	1.3	0.36 ± 0.02
218760.07	H_2CO	3_{21}–2_{20}	4.2	1.5	0.41 ± 0.02
219560.35	$C^{18}O$	$J = 2$–1	4.6	1.0	2.04 ± 0.02
219908.52	$H_2^{13}CO$	3_{12}–2_{11}	4.0	1.1	0.10 ± 0.02
219949.44	SO	6_5–5_4	4.0	1.9	0.89 ± 0.03
VLA 1623 (main)					
216112.58	DCO^+	$J = 3$–2	3.8	0.8	4.85 ± 0.03
216278.76	c-C_3H_2	3_{03}–2_{21}	3.8	0.8	0.45 ± 0.03
216373.32	C_2D	$N = 3$–2, $J = 7/2$–$5/2$[a]	4.0	1.2	0.64 ± 0.03
216428.32	C_2D	$N = 3$–2, $J = 5/2$–$3/2$[b]	3.6	0.8	0.41 ± 0.02
217238.54	DCN	$J = 3$–2	3.8	0.8	0.55 ± 0.03
217822.15	c-C_3H_2	6_{06}–5_{15}, 6_{16}–5_{05}	3.8	0.7	0.52 ± 0.02
217940.05	c-C_3H_2	5_{14}–4_{23}	3.8	0.7	0.34 ± 0.02
218160.46	c-C_3H_2	5_{24}–4_{13}	3.8	0.9	0.09 ± 0.03
218222.19	H_2CO	3_{03}–2_{02}	3.8	0.8	2.57 ± 0.02
218440.06	CH_3OH	4_2–3_1, E	3.7	0.5	0.09 ± 0.02
218475.63	H_2CO	3_{22}–2_{21}	3.7	0.8	0.33 ± 0.02
218760.07	H_2CO	3_{21}–2_{20}	3.8	0.8	0.27 ± 0.02
219560.35	$C^{18}O$	$J = 2$–1	3.9	0.8	13.10 ± 0.02
219908.52	$H_2^{13}CO$	3_{12}–2_{11}	3.8	0.7	0.10 ± 0.02
219949.44	SO	6_5–5_4	3.9	0.7	2.98 ± 0.02
VLA 1623 (secondary)					
218222.19	H_2CO	3_{03}–2_{02}	2.5	1.6	1.46 ± 0.03
218475.63	H_2CO	3_{22}–2_{21}	2.3	1.3	0.16 ± 0.02
218760.07	H_2CO	3_{21}–2_{20}	2.8	1.4	0.14 ± 0.03
219560.35	$C^{18}O$	$J = 2$–1	2.6	1.5	6.26 ± 0.03
219949.44	SO	6_5–5_4	2.3	1.5	1.96 ± 0.03

TABLE 4 — *Continued*

Source Rest freq. [MHz]	Molecule	Transition	$v_{\rm LSR}$ [km s^{-1}]	Δv [km s^{-1}]	$\int T_{\rm mb} dv$ [K km s^{-1}]
ISO-Oph 124 (main)					
216112.58	DCO^+	$J = 3$–2	3.9	0.4	0.24 ± 0.01
218222.19	H_2CO	3_{03}–2_{02}	4.0	1.1	1.71 ± 0.02
218440.06	CH_3OH	4_2–3_1, E	3.9	1.4	0.13 ± 0.02
218475.63	H_2CO	3_{22}–2_{21}	4.7	1.4	0.08 ± 0.02
218760.07	H_2CO	3_{21}–2_{20}	4.3	0.5	0.04 ± 0.01
219560.35	$C^{18}O$	$J = 2$–1	4.2	1.2	12.00 ± 0.02
219949.44	SO	6_5–5_4	4.1	1.0	0.81 ± 0.02
ISO-Oph 124 (secondary)					
216112.58	DCO^+	$J = 3$–2	3.1	0.4	0.10 ± 0.01
218222.19	H_2CO	3_{03}–2_{02}	3.0	0.5	0.76 ± 0.01
218440.06	CH_3OH	4_2–3_1, E	3.1	0.2	0.05 ± 0.01
218475.63	H_2CO	3_{22}–2_{21}	3.2	0.5	0.04 ± 0.01
218760.07	H_2CO	3_{21}–2_{20}	3.1	0.3	0.03 ± 0.01
219560.35	$C^{18}O$	$J = 2$–1	3.1	0.7	3.90 ± 0.02
219949.44	SO	6_5–5_4	3.1	0.4	0.35 ± 0.01
J162728 (main)					
216112.58	DCO^+	$J = 3$–2	4.2	0.5	2.69 ± 0.01
216278.76	c-C_3H_2	3_{03}–2_{21}	4.3	0.4	0.43 ± 0.01
216373.32	C_2D	$N = 3$–2, $J = 7/2$–$5/2$[a]	5.0	0.3	0.07 ± 0.01
216428.32	C_2D	$N = 3$–2, $J = 5/2$–$3/2$[b]	4.3	0.5	0.11 ± 0.01
217238.54	DCN	$J = 3$–2	4.2	0.5	0.12 ± 0.02
217822.15	c-C_3H_2	6_{06}–5_{15}, 6_{16}–5_{05}	4.3	0.4	0.41 ± 0.01
217940.05	c-C_3H_2	5_{14}–4_{23}	4.3	0.5	0.27 ± 0.01
218160.46	c-C_3H_2	5_{24}–4_{13}	4.3	0.4	0.10 ± 0.01
218222.19	H_2CO	3_{03}–2_{02}	4.3	0.6	1.58 ± 0.01
218440.06	CH_3OH	4_2–3_1, E	4.2	0.6	0.07 ± 0.01
218475.63	H_2CO	3_{22}–2_{21}	4.2	0.7	0.09 ± 0.01
218760.07	H_2CO	3_{21}–2_{20}	4.2	0.6	0.06 ± 0.01
219560.35	$C^{18}O$	$J = 2$–1	4.3	0.6	4.43 ± 0.02
219949.44	SO	6_5–5_4	4.2	0.7	0.49 ± 0.02
J162728 (secondary)					
216112.58	DCO^+	$J = 3$–2	3.4	0.5	0.92 ± 0.02
216278.76	c-C_3H_2	3_{03}–2_{21}	3.9	0.5	0.14 ± 0.01
216373.32	C_2D	$N = 3$–2, $J = 7/2$–$5/2$[a]	4.3	0.6	0.17 ± 0.01
216428.32	C_2D	$N = 3$–2, $J = 5/2$–$3/2$[b]	3.4	0.5	0.04 ± 0.01
217822.15	c-C_3H_2	6_{06}–5_{15}, 6_{16}–5_{05}	3.7	0.5	0.07 ± 0.01
217940.05	c-C_3H_2	5_{14}–4_{23}	3.2	0.1	0.01 ± 0.01
218222.19	H_2CO	3_{03}–2_{02}	3.4	0.7	0.93 ± 0.02
218440.06	CH_3OH	4_2–3_1, E	3.2	0.7	0.04 ± 0.02
218475.63	H_2CO	3_{22}–2_{21}	3.3	0.5	0.03 ± 0.01
218760.07	H_2CO	3_{21}–2_{20}	3.5	0.2	0.02 ± 0.01
219560.35	$C^{18}O$	$J = 2$–1	3.1	1.3	8.05 ± 0.02
219949.44	SO	6_5–5_4	3.4	0.5	0.40 ± 0.01
Oph-emb 5					
216112.58	DCO^+	$J = 3$–2	3.9	0.8	2.46 ± 0.02
216278.76	c-C_3H_2	3_{03}–2_{21}	3.9	0.5	0.10 ± 0.01
217822.15	c-C_3H_2	6_{06}–5_{15}, 6_{16}–5_{05}	4.0	1.0	0.08 ± 0.02
217940.05	c-C_3H_2	5_{14}–4_{23}	3.7	0.4	0.04 ± 0.01
218222.19	H_2CO	3_{03}–2_{02}	3.9	1.4	3.17 ± 0.02
218440.06	CH_3OH	4_2–3_1, E	3.8	1.0	0.42 ± 0.02
218475.63	H_2CO	3_{22}–2_{21}	3.7	0.8	0.09 ± 0.02
218760.07	H_2CO	3_{21}–2_{20}	3.7	0.7	0.08 ± 0.02
219560.35	$C^{18}O$	$J = 2$–1	3.7	1.3	9.43 ± 0.03
219908.52	$H_2^{13}CO$	3_{12}–2_{11}	3.8	0.6	0.07 ± 0.02
219949.44	SO	6_5–5_4	3.8	1.1	3.27 ± 0.02
VSSG 17 (main)					
216112.58	DCO^+	$J = 3$–2	4.2	0.6	1.12 ± 0.03
216278.76	c-C_3H_2	3_{03}–2_{21}	4.3	0.6	0.35 ± 0.02
216373.32	C_2D	$N = 3$–2, $J = 7/2$–$5/2$[a]	4.4	1.2	0.12 ± 0.02
216428.32	C_2D	$N = 3$–2, $J = 5/2$–$3/2$[b]	4.2	0.4	0.06 ± 0.02
217238.54	DCN	$J = 3$–2	4.4	0.6	0.06 ± 0.02
217822.15	c-C_3H_2	6_{06}–5_{15}, 6_{16}–5_{05}	4.3	0.5	0.40 ± 0.02
217940.05	c-C_3H_2	5_{14}–4_{23}	4.3	0.4	0.24 ± 0.02
218160.46	c-C_3H_2	5_{24}–4_{13}	4.4	0.6	0.05 ± 0.02
218222.19	H_2CO	3_{03}–2_{02}	4.4	0.8	1.22 ± 0.02
218440.06	CH_3OH	4_2–3_1, E	4.5	0.8	0.04 ± 0.02
218475.63	H_2CO	3_{22}–2_{21}	4.4	1.1	0.11 ± 0.02
218760.07	H_2CO	3_{21}–2_{20}	4.4	0.6	0.06 ± 0.02
219560.35	$C^{18}O$	$J = 2$–1	4.5	1.1	5.80 ± 0.02
219949.44	SO	6_5–5_4	4.5	0.7	0.18 ± 0.02

TABLE 4 — *Continued*

Source Rest freq. [MHz]	Molecule	Transition	$v_{\rm LSR}$ [km s^{-1}]	Δv [km s^{-1}]	$\int T_{\rm mb} dv$ [K km s^{-1}]
VSSG 17 (secondary)					
218222.19	H_2CO	3_{03}–2_{02}	3.3	0.8	0.55 ± 0.02
218440.06	CH_3OH	4_2–3_1, E	3.2	0.5	0.05 ± 0.01
218475.63	H_2CO	3_{22}–2_{21}	3.0	0.4	0.02 ± 0.01
218760.07	H_2CO	3_{21}–2_{20}	3.5	0.5	0.03 ± 0.02
219560.35	$C^{18}O$	$J = 2$–1	3.1	1.2	7.16 ± 0.02
219949.44	SO	6_5–5_4	3.4	0.7	0.11 ± 0.01
WL 2					
217104.98	SiO	$J = 5$–4	6.5	2.2	0.20 ± 0.05
218222.19	H_2CO	3_{03}–2_{02}	3.7	0.5	0.30 ± 0.04
219560.35	$C^{18}O$	$J = 2$–1	3.5	1.3	7.87 ± 0.04
219949.44	SO	6_5–5_4	3.5	2.2	0.32 ± 0.05
WL 12					
216112.58	DCO^+	$J = 3$–2	4.1	0.4	0.13 ± 0.03
218222.19	H_2CO	3_{03}–2_{02}	4.0	0.9	0.28 ± 0.04
219560.35	$C^{18}O$	$J = 2$–1	3.9	1.2	10.10 ± 0.05
219949.44	SO	6_5–5_4	4.1	2.8	0.43 ± 0.06
WL 22					
216112.58	DCO^+	$J = 3$–2	3.7	0.6	0.62 ± 0.02
216278.76	c-C_3H_2	3_{03}–2_{21}	3.7	0.5	0.21 ± 0.02
216373.32	C_2D	$N = 3$–2, $J = 7/2$–$5/2$[a]	3.7	1.2	0.12 ± 0.02
217238.54	DCN	$J = 3$–2	3.8	0.7	0.07 ± 0.02
217822.15	c-C_3H_2	6_{06}–5_{15}, 6_{16}–5_{05}	3.8	0.4	0.10 ± 0.01
217940.05	c-C_3H_2	5_{14}–4_{23}	3.8	0.2	0.07 ± 0.01
218160.46	c-C_3H_2	5_{24}–4_{13}	4.1	0.8	0.08 ± 0.02
218222.19	H_2CO	3_{03}–2_{02}	3.8	0.8	0.75 ± 0.03
218440.06	CH_3OH	4_2–3_1, E	3.9	0.6	0.06 ± 0.02
219560.35	$C^{18}O$	$J = 2$–1	...	...	Off-em.
219949.44	SO	6_5–5_4	3.9	0.7	0.45 ± 0.01
[GY92] 197					
216112.58	DCO^+	$J = 3$–2	4.8	0.3	0.08 ± 0.02
218222.19	H_2CO	3_{03}–2_{02}	4.8	0.9	0.34 ± 0.03
219560.35	$C^{18}O$	$J = 2$–1	...	...	Off-em.
219949.44	SO	6_5–5_4	4.8	2.8	0.29 ± 0.04
WL 15					
216112.58	DCO^+	$J = 3$–2	4.6	0.6	0.10 ± 0.03
218222.19	H_2CO	3_{03}–2_{02}	4.5	2.2	0.44 ± 0.05
219560.35	$C^{18}O$	$J = 2$–1	...	...	Off-em.
219949.44	SO	6_5–5_4	4.9	2.3	1.78 ± 0.06
WL 16					
219560.35	$C^{18}O$	$J = 2$–1	...	...	Off-em.
WL 17					
218222.19	H_2CO	3_{03}–2_{02}	4.6	0.9	0.23 ± 0.04
219560.35	$C^{18}O$	$J = 2$–1	...	...	Off-em.
219949.44	SO	6_5–5_4	4.6	0.4	0.09 ± 0.03
IRAS 16244-2432					
218222.19	H_2CO	3_{03}–2_{02}	3.7	1.9	0.51 ± 0.05
219560.35	$C^{18}O$	$J = 2$–1	...	...	Off-em.
219949.44	SO	6_5–5_4	3.8	4.2	1.83 ± 0.07
IRAS 16246-2436					
216112.58	DCO^+	$J = 3$–2	3.6	0.4	0.50 ± 0.02
216278.76	c-C_3H_2	3_{03}–2_{21}	3.7	0.3	0.07 ± 0.01
218222.19	H_2CO	3_{03}–2_{02}	3.7	0.6	0.53 ± 0.02
218440.06	CH_3OH	4_2–3_1, E	3.7	0.6	0.09 ± 0.01
219560.35	$C^{18}O$	$J = 2$–1	3.7	0.7	3.86 ± 0.02
219949.44	SO	6_5–5_4	3.7	0.4	0.29 ± 0.01
ISO-Oph 132					
216112.58	DCO^+	$J = 3$–2	4.0	0.3	0.26 ± 0.03
218222.19	H_2CO	3_{03}–2_{02}	4.0	0.3	0.18 ± 0.02
219560.35	$C^{18}O$	$J = 2$–1	...	...	Off-em.
ISO-Oph 137					
216112.58	DCO^+	$J = 3$–2	4.0	0.4	1.54 ± 0.04
216278.76	c-C_3H_2	3_{03}–2_{21}	4.0	0.2	0.18 ± 0.02
216373.32	C_2D	$N = 3$–2, $J = 7/2$–$5/2$[a]	4.6	1.2	0.21 ± 0.04
217238.54	DCN	$J = 3$–2	4.1	0.5	0.18 ± 0.03
217822.15	c-C_3H_2	6_{06}–5_{15}, 6_{16}–5_{05}	3.9	0.2	0.07 ± 0.02
218222.19	H_2CO	3_{03}–2_{02}	4.4	1.3	0.94 ± 0.04
218440.06	CH_3OH	4_2–3_1, E	4.7	0.2	0.05 ± 0.02
219560.35	$C^{18}O$	$J = 2$–1	4.3	1.6	10.50 ± 0.05

TABLE 4 — *Continued*

Source Rest freq. [MHz]	Molecule	Transition	$v_{\rm LSR}$ [km s^{-1}]	Δv [km s^{-1}]	$\int T_{\rm mb} dv$ [K km s^{-1}]
219949.44	SO	6_5–5_4	4.8	0.5	0.07 ± 0.02
ISO-Oph 161					
216112.58	DCO^+	$J = 3$–2	3.6	0.4	0.95 ± 0.03
216278.76	c-C_3H_2	3_{03}–2_{21}	3.7	0.4	0.13 ± 0.03
218222.19	H_2CO	3_{03}–2_{02}	3.8	0.6	0.59 ± 0.04
219560.35	$C^{18}O$	$J = 2$–1	...	...	Off-em.
219949.44	SO	6_5–5_4	3.8	0.5	0.20 ± 0.03
YLW 15					
216112.58	DCO^+	$J = 3$–2	4.1	0.4	0.87 ± 0.03
216278.76	c-C_3H_2	3_{03}–2_{21}	4.1	0.4	0.23 ± 0.03
217238.54	DCN	$J = 3$–2	4.3	1.0	0.10 ± 0.03
217822.15	c-C_3H_2	6_{06}–5_{15}, 6_{16}–5_{05}	4.1	0.4	0.14 ± 0.02
218222.19	H_2CO	3_{03}–2_{02}	3.9	2.4	1.12 ± 0.05
219560.35	$C^{18}O$	$J = 2$–1	4.1	1.9	11.20 ± 0.06
IRAS 16293-2422 (main)					
216112.58	DCO^+	$J = 3$–2	4.5	1.1	3.62 ± 0.02
216278.76	c-C_3H_2	3_{03}–2_{21}	4.6	1.3	0.75 ± 0.02
216373.32	C_2D	$N = 3$–2, $J = 7/2$–$5/2$[a]	4.4	2.2	0.67 ± 0.02
216428.32	C_2D	$N = 3$–2, $J = 5/2$–$3/2$[b]	4.0	1.8	0.33 ± 0.02
216570.33	^{13}CN	$N = 2$–1, $J = 3/2$–$3/2$[d]	4.9	1.3	0.28 ± 0.03
216643.30	SO_2	$22_{2,20}$–$22_{1,21}$	5.5	2.9	0.31 ± 0.03
216662.43	HDCS	7_{07}–6_{06}	4.0	1.9	0.14 ± 0.02
216945.56	CH_3OH	5_{14}–4_{22}	4.6	3.4	0.53 ± 0.03
217104.98	SiO	$J = 5$–4	4.8	5.2	5.10 ± 0.05
217238.54	DCN	$J = 3$–2	5.0	1.4	0.95 ± 0.02
217301.18	^{13}CN	$N = 2$–1, $J = 3/2$–$1/2$[e]	4.0	6.9	0.62 ± 0.05
217428.56	^{13}CN	$N = 2$–1, $J = 5/2$–$3/2$[f]	4.5	5.9	0.25 ± 0.04
217469.15	^{13}CN	$N = 2$–1, $J = 5/2$–$3/2$[g]	2.1	2.7	0.28 ± 0.03
217822.15	c-C_3H_2	6_{06}–5_{15}, 6_{16}–5_{05}	4.6	1.3	1.26 ± 0.02
217886.39	CH_3OH	20_1–20_0, E1	3.3	4.1	0.19 ± 0.03
217940.05	c-C_3H_2	5_{14}–4_{23}	4.7	1.1	0.57 ± 0.02
218160.46	c-C_3H_2	5_{24}–4_{13}	4.7	1.9	0.35 ± 0.02
218222.19	H_2CO	3_{03}–2_{02}	4.8	2.0	7.37 ± 0.02
218324.72	HC_3N	$J = 24$–23	3.9	3.7	0.62 ± 0.03
218440.06	CH_3OH	4_2–3_1, E	4.1	3.5	2.62 ± 0.03
218475.63	H_2CO	3_{22}–2_{21}	4.7	2.7	2.36 ± 0.02
218732.73	c-C_3H_2	7_{16}–7_{07}, 7_{26}–7_{17}	4.6	3.8	0.20 ± 0.03
218760.07	H_2CO	3_{21}–2_{20}	5.1	2.8	1.43 ± 0.02
218903.36	OCS	18–17	3.5	5.7	2.12 ± 0.04
219355.01	$^{34}SO_2$	$11_{1,11}$–$10_{0,10}$	4.0	2.7	0.18 ± 0.03
219560.35	$C^{18}O$	$J = 2$–1	4.5	1.6	12.46 ± 0.02
219908.52	$H_2^{13}CO$	3_{12}–2_{11}	5.0	1.5	0.13 ± 0.02
219949.44	SO	6_5–5_4	4.6	4.3	16.63 ± 0.03
IRAS 16293-2422 (secondary)					
216112.58	DCO^+	$J = 3$–2	3.3	1.2	0.85 ± 0.02
216278.76	c-C_3H_2	3_{03}–2_{21}	3.4	1.7	0.20 ± 0.02
216435.28	CH_3CHO	$16_{2,15}$–$16_{1,16}$, A	2.7	1.2	0.06 ± 0.01
216534.36	CH_3CHO	$14_{3,11}$–$14_{2,12}$, E	2.7	1.8	0.10 ± 0.02
216581.93	CH_3CHO	$11_{1,10}$–$10_{1,9}$, E	3.2	2.7	0.15 ± 0.02
216630.23	CH_3CHO	$11_{1,10}$–$10_{1,9}$, A	3.3	3.1	0.22 ± 0.02
216643.30	SO_2	$22_{2,20}$–$22_{1,21}$	2.2	4.5	0.50 ± 0.04
216710.44	H_2S	2_{20}–2_{11}	3.4	4.6	3.08 ± 0.04
216830.15	CH_3OCHO	$18_{2,16}$–$17_{2,15}$, E	3.3	6.6	0.27 ± 0.03
216945.56	CH_3OH	5_{14}–4_{22}	2.6	2.8	0.41 ± 0.03
216967.42	CH_3OCHO	$20_{0,20}$–$19_{0,19}$, A	4.4	9.9	0.92 ± 0.04
217191.42	CH_3OCH_3	–	2.7	6.0	0.39 ± 0.04
217238.54	DCN	$J = 3$–2	3.2	1.3	1.15 ± 0.02
217822.15	c-C_3H_2	6_{06}–5_{15}, 6_{16}–5_{05}	3.1	1.4	0.42 ± 0.02
217886.39	CH_3OH	20_1–20_0, E1	-0.0	2.7	0.13 ± 0.03
217940.05	c-C_3H_2	5_{14}–4_{23}	3.6	1.9	0.41 ± 0.02
218160.46	c-C_3H_2	5_{24}–4_{13}	2.6	0.8	0.07 ± 0.01
218222.19	H_2CO	3_{03}–2_{02}	3.2	1.1	5.05 ± 0.02
218297.89	CH_3OCHO	$17_{3,14}$–$16_{3,13}$, A	1.8	2.2	0.13 ± 0.03
218324.72	HC_3N	$J = 24$–23	0.8	0.9	0.07 ± 0.01
218440.06	CH_3OH	4_2–3_1, E	0.3	2.0	0.19 ± 0.02
218475.63	H_2CO	3_{22}–2_{21}	3.2	1.7	1.04 ± 0.02
218654.66	CH_3OCHO	$18_{16,2}$–$17_{16,1}$, E	3.3	2.9	0.10 ± 0.02
218732.73	c-C_3H_2	7_{16}–7_{07}, 7_{26}–7_{17}	2.4	1.7	0.02 ± 0.02
218760.07	H_2CO	3_{21}–2_{20}	3.5	2.8	2.33 ± 0.02
218903.36	OCS	18–17	2.5	1.1	0.24 ± 0.02
218981.02	HNCO	$10_{1,10} - 9_{1,9}$	3.8	7.9	0.57 ± 0.04
219355.01	$^{34}SO_2$	$11_{1,11}$–$10_{0,10}$	1.3	1.9	0.06 ± 0.02

TABLE 4 — *Continued*

Source Rest freq. [MHz]	Molecule	Transition	$v_{\rm LSR}$ [km s^{-1}]	Δv [km s^{-1}]	$\int T_{\rm mb} dv$ [K km s^{-1}]
219560.35	$C^{18}O$	$J = 2$–1	3.1	1.3	7.70 ± 0.02
219656.80	HNCO	10_{38}–9_{37}, 10_{37}–9_{36}	2.8	2.6	0.11 ± 0.02
219737.19	HNCO	10_{28}–9_{27}	6.3	10.1	0.64 ± 0.04
219798.27	HNCO	$10_{0,10}$–$9_{0,9}$	3.9	5.1	1.12 ± 0.03
219820.39	CH_3CHO	$4_{-2,3}$–$3_{-1,3}$, E	2.8	2.1	0.10 ± 0.02
219908.52	$H_2^{13}CO$	3_{12}–2_{11}	3.3	2.6	0.58 ± 0.02
219949.44	SO	6_5–5_4	3.6	1.5	4.79 ± 0.02
ISO-Oph 200					
216112.58	DCO^+	$J = 3$–2	4.7	0.5	0.26 ± 0.03
218222.19	H_2CO	3_{03}–2_{02}	4.7	0.8	0.70 ± 0.03
219560.35	$C^{18}O$	$J = 2$–1	4.7	0.9	4.55 ± 0.04
219949.44	SO	6_5–5_4	4.7	0.9	0.48 ± 0.03
ISO-Oph 202					
218222.19	H_2CO	3_{03}–2_{02}	4.6	0.8	0.55 ± 0.04
219560.35	$C^{18}O$	$J = 2$–1	4.6	0.7	3.59 ± 0.04
219949.44	SO	6_5–5_4	4.8	0.5	0.15 ± 0.03
ISO-Oph 203 (main)					
216112.58	DCO^+	$J = 3$–2	4.4	0.4	0.45 ± 0.01
216278.76	c-C_3H_2	3_{03}–2_{21}	4.5	0.4	0.19 ± 0.01
216373.32	C_2D	$N = 3$–2, $J = 7/2$–$5/2$[a]	4.5	1.0	0.12 ± 0.02
216428.32	C_2D	$N = 3$–2, $J = 5/2$–$3/2$[b]	4.3	0.4	0.05 ± 0.01
217822.15	c-C_3H_2	6_{06}–5_{15}, 6_{16}–5_{05}	4.4	0.5	0.14 ± 0.01
217940.05	c-C_3H_2	5_{14}–4_{23}	4.4	0.4	0.10 ± 0.01
218222.19	H_2CO	3_{03}–2_{02}	4.5	0.6	0.61 ± 0.01
218440.06	CH_3OH	4_2–3_1, E	4.6	0.6	0.04 ± 0.01
218475.63	H_2CO	3_{22}–2_{21}	4.3	0.3	0.01 ± 0.01
218760.07	H_2CO	3_{21}–2_{20}	4.5	0.5	0.05 ± 0.01
219560.35	$C^{18}O$	$J = 2$–1	4.5	0.7	5.63 ± 0.02
219949.44	SO	6_5–5_4	4.3	0.4	0.04 ± 0.01
ISO-Oph 203 (secondary)					
216112.58	DCO^+	$J = 3$–2	4.8	0.4	0.32 ± 0.01
218222.19	H_2CO	3_{03}–2_{02}	5.0	0.4	0.40 ± 0.01
218440.06	CH_3OH	4_2–3_1, E	5.0	0.2	0.02 ± 0.01
218475.63	H_2CO	3_{22}–2_{21}	4.7	0.7	0.04 ± 0.01
218760.07	H_2CO	3_{21}–2_{20}	4.9	0.3	0.02 ± 0.01
219560.35	$C^{18}O$	$J = 2$–1	4.9	0.3	0.76 ± 0.01
219949.44	SO	6_5–5_4	4.9	0.4	0.20 ± 0.01
ISO-Oph 209					
216112.58	DCO^+	$J = 3$–2	4.2	0.5	0.32 ± 0.04
217822.15	c-C_3H_2	6_{06}–5_{15}, 6_{16}–5_{05}	2.9	1.3	0.18 ± 0.05
218222.19	H_2CO	3_{03}–2_{02}	4.2	1.3	0.48 ± 0.04
219560.35	$C^{18}O$	$J = 2$–1	4.4	1.3	3.42 ± 0.06
219949.44	SO	6_5–5_4	4.6	3.2	0.35 ± 0.07
GWAYL 4					
216112.58	DCO^+	$J = 3$–2	2.7	0.3	0.18 ± 0.03
217822.15	c-C_3H_2	6_{06}–5_{15}, 6_{16}–5_{05}	3.0	1.3	0.14 ± 0.04
218222.19	H_2CO	3_{03}–2_{02}	2.8	0.5	0.41 ± 0.03
219560.35	$C^{18}O$	$J = 2$–1	2.7	0.6	4.76 ± 0.04
219949.44	SO	6_5–5_4	3.0	1.8	0.54 ± 0.05
Oph-emb 4					
219560.35	$C^{18}O$	$J = 2$–1	2.6	0.5	3.21 ± 0.04
Elias 28					
219560.35	$C^{18}O$	$J = 2$–1	4.2	1.0	1.27 ± 0.06
J162624					
218222.19	H_2CO	3_{03}–2_{02}	3.3	0.8	0.33 ± 0.03
219560.35	$C^{18}O$	$J = 2$–1	...	...	Off-em.
219949.44	SO	6_5–5_4	3.5	0.9	0.41 ± 0.04
J1633.92442					
No lines detected					
MMS126					
216112.58	DCO^+	$J = 3$–2	4.0	0.5	1.16 ± 0.02
216278.76	c-C_3H_2	3_{03}–2_{21}	4.0	0.5	0.42 ± 0.02
216373.32	C_2D	$N = 3$–2, $J = 7/2$–$5/2$[a]	4.2	1.0	0.08 ± 0.02
217238.54	DCN	$J = 3$–2	4.2	0.6	0.06 ± 0.02
217822.15	c-C_3H_2	6_{06}–5_{15}, 6_{16}–5_{05}	4.1	0.4	0.28 ± 0.02
217940.05	c-C_3H_2	5_{14}–4_{23}	4.1	0.3	0.19 ± 0.01
218160.46	c-C_3H_2	5_{24}–4_{13}	4.1	0.2	0.05 ± 0.01
218222.19	H_2CO	3_{03}–2_{02}	4.1	0.4	0.88 ± 0.02
218440.06	CH_3OH	4_2–3_1, E	3.6	1.0	0.08 ± 0.02

TABLE 4 — *Continued*

Source Rest freq. [MHz]	Molecule	Transition	$v_{\rm LSR}$ [km s^{-1}]	Δv [km s^{-1}]	$\int T_{\rm mb} dv$ [K km s^{-1}]
219560.35	$C^{18}O$	$J = 2$–1	4.1	0.9	4.45 ± 0.02
219908.52	$H_2^{13}CO$	3_{12}–2_{11}	4.4	2.6	0.13 ± 0.03
219949.44	SO	6_5–5_4	4.2	0.5	0.23 ± 0.02
Oph-emb 18					
218222.19	H_2CO	3_{03}–2_{02}	3.5	0.2	0.06 ± 0.02
218440.06	CH_3OH	4_2–3_1, E	2.0	3.8	0.18 ± 0.05
219560.35	$C^{18}O$	$J = 2$–1	3.5	0.5	3.97 ± 0.03

NOTE. — Rest frequencies from the CDMS (Müller et al. 2001) and JPL (Pickett et al. 1998) molecular spectroscopy databases.

[a] Blend of $F = 9/2$–$7/2$, $F = 7/2$–$5/2$, and $F = 5/2$–$3/2$.
[b] Blend of $F = 7/2$–$5/2$, $F = 5/2$–$3/2$, and $F = 3/2$–$1/2$.
[c] Blend of $F = 13/2$–$11/2$ and $F = 15/2$–$13/2$.
[d] $F_1 = 2$–$2, F = 2$–1.
[e] $F_1 = 2$–$1, F = 2$–1.
[f] $F_1 = 2$–$1, F = 3$–2.
[g] $F_1 = 3$–$2, F = 2$–1.

B. SPECTRAL LINE PROFILES IN CORONA AUSTRALIS SOURCES

For completeness, Figure 8 shows the spectral profiles of the sources in the CrA survey of embedded protostars (Lindberg et al. 2015) by plotting the normalized spectra for the strongest DCO^+ (216.113 GHz), c-C_3H_2 (217.822 GHz), H_2CO (218.222 GHz), and SO (219.949 GHz) lines in each source where they have been detected (cf. Figure 3).

C. NON-LTE ANALYSIS OF c-C_3H_2

In our observations, the rotational temperatures of c-C_3H_2 were generally found to be lower than those of H_2CO. To verify that this reflects a difference in physical temperatures and is not just a non-LTE or optical depth effect, we used the radiative transfer code RADEX (van der Tak et al. 2007) to study line ratios within a range of physical parameters. A similar investigation of the H_2CO rotational temperature was performed by Mangum & Wootten (1993), showing that a rotational temperature calculated from H_2CO transitions with the same J_u will provide a good measure of the physical temperature.

We here use RADEX to calculate non-LTE line ratios of four of the five c-C_3H_2 lines covered in our observations (see Table 2; the 218.733 GHz line is not included since it is only detected toward one source). One of these lines is a

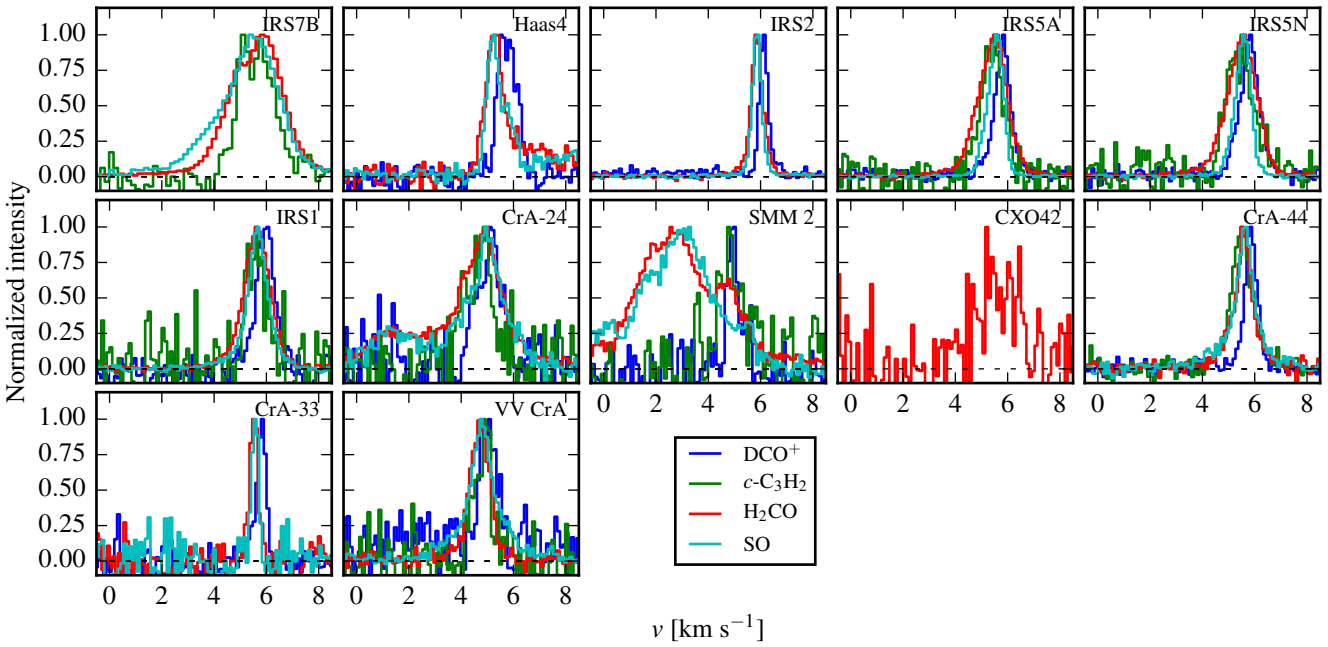

FIG. 8.— Normalized spectra of the DCO^+ (216.113 GHz), c-C_3H_2 (217.822 GHz), H_2CO (218.222 GHz), and SO (219.949 GHz) lines for all sources in the CrA survey of embedded protostars (Lindberg et al. 2015) for which at least one of these lines is detected at a 3σ level or higher (CrA-3, CrA-5, LS-RCrA1, CrA-37, and CrA-46 are thus not included). The DCO^+ line was not covered by the R CrA IRS7B observations.

blend between an ortho and a para line, two lines are ortho lines, and the final one is a para line. Excitation analysis involving a combination of ortho and para lines will therefore depend on the assumed ortho-to-para ratio. For c-C_3H_2, we use a ratio of 3 (Lucas & Liszt 2000). We use the collisional rates of Chandra & Kegel (2000) retrieved from the LAMDA database (Schöier et al. 2005).

Since three of the four lines have roughly the same upper level energy (E_u = 35–39 K), we only show ratios between the 216.279 GHz line (E_u = 19.5 K) and the remaining three lines. We perform the non-LTE calculations assuming three different column densities (total ortho+para c-C_3H_2 column densities): $N = 10^{12}$ cm^{-2}, $N = 10^{13}$ cm^{-2}, and $N = 10^{14}$ cm^{-2}. Our observations show that the c-C_3H_2 column densities typically are $< 10^{13}$ cm^{-2}, so the $N = 10^{14}$ cm^{-2} case is unlikely to be applicable to this work. A model with $N = 10^{11}$ cm^{-2} (not plotted) has results identical to the $N = 10^{12}$ cm^{-2} model. The results are shown in Figure 9.

We find that the 216.279 GHz/217.822 GHz non-LTE line ratio is within $\sim$ 5 K of the LTE solution given $T_{kin} \lesssim 20$ K for all densities and column densities. The other two ratios are worse off in predicting the temperature, in particular for low H_2 densities. At $T_{kin} \lesssim 20$ K and $n(H_2) \gtrsim 5 \times 10^5$ cm^{-3}, the temperature is, however, only under-predicted (or over-predicted) by $\lesssim 5$ K. Densities are expected to exceed 5×10^5 cm^{-3} within the inner 1800 au of a majority of embedded protostars (e.g. Jørgensen et al. 2002), which is the radius of the APEX beam projected to the distance of the Ophiuchus cloud (125 pc).

We compare the rotational (LTE) temperatures calculated when using only the 216.279 GHz and the 217.822 GHz lines with those calculated from using all detected lines for all sources in the sample, and find that in no source the difference is greater than 2 K. The rotational temperatures of c-C_3H_2 presented in Table 3 use all observed c-C_3H_2 lines, and might thus be under-estimated, but calculating rotational temperatures from RADEX intensities shows that this difference is $\lesssim 5$ K. We therefore conclude that the physical temperature of the c-C_3H_2 gas is significantly lower than that of the H_2CO gas in the externally irradiated sources in the sample.

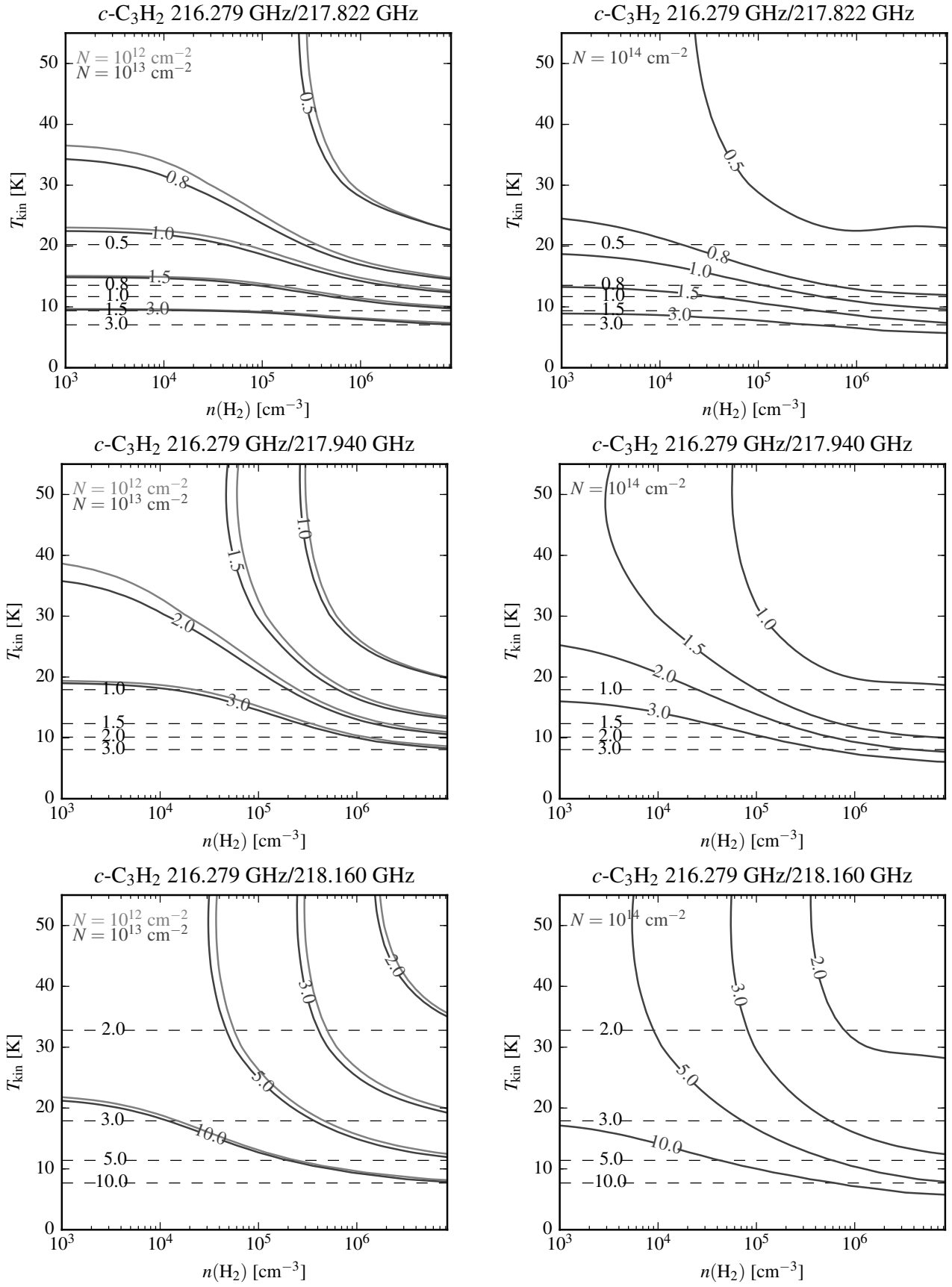

FIG. 9.— c-C_3H_2 line ratios assuming LTE (dashed lines) and with non-LTE RADEX models (solid lines).